Naval Research Laboratory
Washington, DC 20375-5320

NRL/MR/6410--03-8658

Blast Mitigation by Water Mist 2) Shock Wave Mitigation Using Glass Particles and Water Droplets in Shock Tubes

DOUGLAS SCHWER
K. KAILASANATH

Center for Reactive Flow and Dynamical Systems
Laboratory for Computational Physics and Fluid Dynamics

January 21, 2003

REPORT DOCUMENTATION PAGE

Form Approved
OMB No. 0704-0188

1. REPORT DATE *(DD-MM-YYYY)*	2. REPORT TYPE	3. DATES COVERED *(From - To)*
January 21, 2003	NRL Memorandum Report	

4. TITLE AND SUBTITLE

Blast Mitigation by Water Mist
2) Shock Wave Mitigation Using Glass Particles and Water Droplets in Shock Tubes

5a. CONTRACT NUMBER

5b. GRANT NUMBER
64-1530-02

5c. PROGRAM ELEMENT NUMBER

6. AUTHOR(S)

Douglas Schwer and K. Kailasanath

5d. PROJECT NUMBER

5e. TASK NUMBER

5f. WORK UNIT NUMBER

7. PERFORMING ORGANIZATION NAME(S) AND ADDRESS(ES)

Naval Research Laboratory
4555 Overlook Avenue, SW
Washington, DC 20375-5320

8. PERFORMING ORGANIZATION REPORT NUMBER

NRL/MR/6410--03-8658

9. SPONSORING / MONITORING AGENCY NAME(S) AND ADDRESS(ES)

10. SPONSOR / MONITOR'S ACRONYM(S)

11. SPONSOR / MONITOR'S REPORT NUMBER(S)

12. DISTRIBUTION / AVAILABILITY STATEMENT

Approved for public release; distribution is unlimited.

13. SUPPLEMENTARY NOTES

14. ABSTRACT

This report is the second in a series of reports discussing mitigation of blasts using water mists. The previous report described numerical simulations of a TNT blast. The present report has combined that numerical procedure with a two-continuum model for dispersed-phase calculations. The specific approach used for the dispersed-phase calculations is the sectional approach, and is described in this report along with a series of simulations conducted for validation, and also for the purpose of better understanding interactions between shock waves and particle-seeded gases.

15. SUBJECT TERMS

Blast mitigation; Damage control; Water-mist suppression; Shock suppression; Explosions; Modeling and simulation

16. SECURITY CLASSIFICATION OF:			17. LIMITATION OF ABSTRACT	18. NUMBER OF PAGES	19a. NAME OF RESPONSIBLE PERSON
a. REPORT	b. ABSTRACT	c. THIS PAGE			Douglas Schwer
Unclassified	Unclassified	Unclassified	UL	61	19b. TELEPHONE NUMBER *(include area code)* (202) 767-3615

Standard Form 298 (Rev. 8-98)
Prescribed by ANSI Std. Z39.18

This Page Intentionaly
Left Blank

Contents

List of Tables

List of Figures

This Page Intentionaly
Left Blank

Abstract

This report is the second in a series of reports discussing mitigation of blasts using water mists. The previous report described numerical simulations of a TNT blast. The present report has combined that numerical procedure with a two-continuum model for dispersed-phase calculations. The specific approach used for the dispersed-phase calculations is the sectional approach, and is described in this report along with a series of simulations conducted for validation, and also for the purpose of better understanding interactions between shock waves and particle-seeded gases.

A new derivation of the sectional approach is presented in this report to provide details and to outline the limitations of this approach. This approach is then incorporated into a flux-corrected-transport high speed flow code, and is used to examine mitigation characteristics of glass particles and water droplets on impinging shock waves. First a series of validation cases are presented comparing simulations against available experiments. Results show that the present solution technique accurately predicts the shock wave behavior in particle-seeded gases. Further simulations were conducted to investigate the effect of particle size and vaporization for both non-decaying and decaying shocks. For steady shock waves, it was determined that for finite-sized particles, the shock front pressure and maximum overpressure are not equal, with the shock front pressure typically being smaller than the unmitigated shock pressure, and the maximum overpressure being greater than the unmitigated shock pressure for non-decaying shocks, dependent primarily on the mass-loading of the particles. For decaying shock waves, there is an optimum particle size which gives the most effective mitigation for the peak overpressure, but is specific to the shock tube geometry considered. Vaporization effects tended to be minimal for the cases presented in this report, because the shock waves were fairly weak resulting in only moderate temperatures for the shocked driven gases. Blasts tend to be similar to the decaying shock wave solutions, except that they are considerably more powerful, and should have high enough temperatures such that vaporization will play a more significant role in mitigation.

BLAST MITIGATION BY WATER MIST
2) SHOCK WAVE MITIGATION USING GLASS PARTICLES AND WATER DROPLETS IN SHOCK TUBES

1 Introduction

Explosions and fires have always represented a danger to naval ships. Large amounts of fuel and ordnance on-board these ships provide plentiful fuel for explosions and fires even in peacetime. Recent events such as the USS Cole have highlighted the need to be able to mitigate the effects of explosions on board ships, whether caused by internal or external factors.

Several recent studies have looked at water to mitigate the effects of explosions. Using water is attractive for several reasons. The large heat capacity and latent heat of vaporization allows water to easily absorb a large amount of energy. In addition, water systems have a great deal of flexibility and low cost, are environmentally safe and clean to use, and can serve a dual role of fire suppression in peacetime situations and explosion mitigation during war and terrorist situations. A recent summary of efforts to use water and water mist systems to mitigate the effects of blasts and explosions is given in [1].

Of particular interest for the current project is mitigation of the initial and quasi-steady overpressures felt within an enclosure that is subjected to an explosive blast. Previous studies [2] demonstrated that the blast characteristics within simple enclosures for 2.12 kg of TNT could be effectively simulated, reproducing overpressures and quasi-static pressures that were similar to experimental results [3]. The next step is to develop a spray model and incorporate it into the blast simulation, to determine the amount of actual mitigation effected by the water spray.

There has been a substantial amount of research on spray models within the literature. Sirignano [4] provides a review of currently popular models and details of useful solution procedures. However, the majority of these spray and particle models have been developed for low speed flows such as occurring in engines or fire situations. There is unfortunately relatively little information on the effect of an impinging shock wave on vaporization of water or fuel droplets, although some work has been done investigating droplet breakup processes when exposed to an impinging shock wave [5, 6]. These results are for substantially larger droplets than our current interest.

The intent of this report is to describe the spray model that will be used for the subsequent blast mitigation studies, and use this model to characterize shock tube flow where the driven section is seeded with glass particles and water droplets. One-dimensional shock tube simulations were chosen because shock tubes have

Manuscript approved December 3, 2002.

many similarities with explosive blasts, but are simple enough that concurrent experimental studies can also be done by interested researchers. In addition, some experimental studies with particles have already been done without vaporization [7]. Of particular interest for our numerical simulations is the reduction in shock wave speed and the maximum overpressure felt for different configurations at different locations in the shock tube. These are the two main quantities that can be easily compared with experimental results.

2 Transmission of Shock Waves through Particle-Seeded Gases

Due to the importance of "dusty" gases (gases seeded with particles that occupy only a small fraction of the volume but have a significant mass), there has been a considerable amount of research on the transmission of shock waves through particle-seeded flows. For this report, we are interested in how particles and droplets affect the pressure and temperature developed behind the shock wave as well as the velocity of the shock wave.

The first step is to understand how the particles affect a typical shock wave as it penetrates from an unseeded (pure) gas into a particle-seeded gas. The shock wave essentially hits a material interface as it passes into the particle-seeded gas. As happens at most material interfaces, depending on the properties of the particles, the shock wave is transmitted through the interface and a reflected wave propagates back into the initial (unseeded) mixture as shown in Figure 1 for infinitely small particles. Depending on the material properties of the gas mixtures on either side of the reflected wave, the wave can either be a compressive wave ($u_{2'} < u_2$) or a rarefaction wave ($u_{2'} > u_2$). For the types of particles considered in this paper, compressive reflected shocks are generated resulting in lower gas velocities $u_{2'} < u_2$ and higher pressures $P_{2'} > P_2$. For particles of finite size, the $x-t$ diagram shown in Figure 1 requires some slight modifications that are discussed later. We are interested in determining the pressure $P_{2'}$ between the reflected wave and the transmitted shock wave.

For particles that do not evaporate or sublimate, a useful limit that allows analysis of the situation shown in Figure 1 is the limit as the particles become infinitely small. In this case, the particles remain in equilibrium with the surrounding gas and an "equivalent" gas formulation can be used [8]. For the equivalent gas, the total density is represented as $\rho_t = \rho(1 + \eta)$, where ρ is the gas density, and η is the mass-loading.

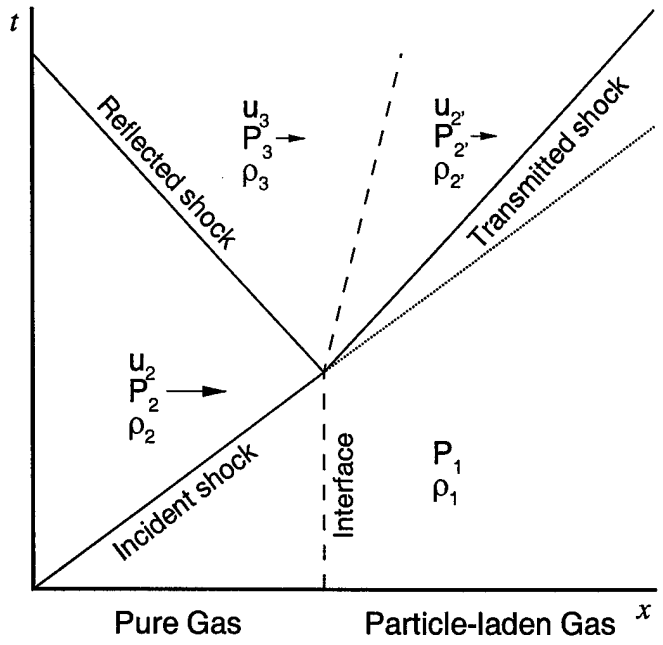

Figure 1: $x - t$ diagram of shock wave from an unseeded (pure) gas impinging on a particle-seeded gas. The dashed line shows the material interface separating the unseeded and the seeded gas, and the dotted line is a continuation of the incident shock wave for the unseeded gas.

The pressure is computed using the ideal gas law with the gas density and temperature, and the enthalpy of the equivalent gas is given by $H = \rho(1 + \eta c)C_p T$, where C_p is the gas specific heat, and c is the ratio of specific heats between the solid particles and gas ($c = C_s/C_p$).

By using these definitions, we develop expressions for the (P, v) Hugoniot and the (P, u) Hugoniot for particle-seeded flows that are useful for understanding the transmission of shocks through material interfaces, where v is the specific gas volume ($v = 1/\rho$). The Hugoniot expressions are developed assuming a single steady shock wave and considering mass, momentum, and energy conservation through the shock. For ideal, calorically perfect gases (meaning that the specific heat is constant and independent of temperature and pressure), the (P, v) Hugoniot for a particle-seeded flow is:

$$\frac{\gamma}{\gamma - 1}(1 + \eta c)[P_2 v_2 - P_1 v_1] = \frac{1}{2}(P_2 - P_1)(v_1 + v_2) \tag{1}$$

where γ is the specific heat ratio of the pure gas. P_1, v_1 are the unshocked pressure and gas-phase specific volume respectively, and P_2, v_2 are the shocked pressure and gas-phase specific volumes. Another Hugoniot

expression useful for shock wave interactions with material interfaces is the (P, u) Hugoniot, where u is the velocity in the lab reference frame:

$$\frac{(P_2 - P_1)^2}{(\mathcal{A} + 1/2)(P_2 - P_1) + \mathcal{A}P_1} = \frac{1+\eta}{\mathcal{A}v_1}(u_2 - u_1)^2 \tag{2}$$

where $\mathcal{A} = \frac{\gamma}{\gamma - 1}(1 + \eta c)$. These quantities can be related to the shock wave velocity through the Raleigh line, which is developed from a manipulation of the mass and momentum conservation equations:

$$\gamma M^2 = \left(\frac{1}{1+\eta}\right)\frac{P_2/P_1 - 1}{1 - v_2/v_1} \tag{3}$$

where M is the Mach number of the shock wave with respect to the pure unshocked gas. The Hugoniot expressions along with the Raleigh expression are extremely useful when determining the characteristics of shocks. Using these expressions, one can determine the pressure increase or decrease resulting from a shock wave impinging on a particle-seeded gas, knowing that the pressure and velocity in section 2' and 3 from Figure 1 are equal.

Results from this analysis are shown in Figure 2. This figure specifically looks at the effect of seeding with glass particles in air. Notable among the results is that the shock pressure is actually increased for the seeded flow (Fig. 2b) while the velocity of the shock wave and the shocked gases (Figs. 2a and 2d) decreases. Non-vaporizing water droplets have a similar impact on the shock wave velocity and shock pressure; however, the effect of vaporization is difficult to account for in such a simplified analysis.

Particle seeding of gases to mitigate the pressure associated with steady shocks is shown to be ineffectual from the above plots. However, explosions are typically more complex than the simple steady shock. A representative geometry that more closely approximates an actual blast is a shock tube experimental setup with a small driver section. Shock tubes have been used extensively to understand different aspects of shock waves and rarefaction waves. They provide an ideal experimental setup because the flow is largely one-dimensional and thus facilitates mathematical modeling.

A shock tube is made up of a cylindrical or rectangular pipe divided into two compartments separated by a diaphragm of thin material as shown in Figure 3. The smaller compartment contains gas at high pressure and is called the driver section. The larger compartment is called the driven section and contains a gas at

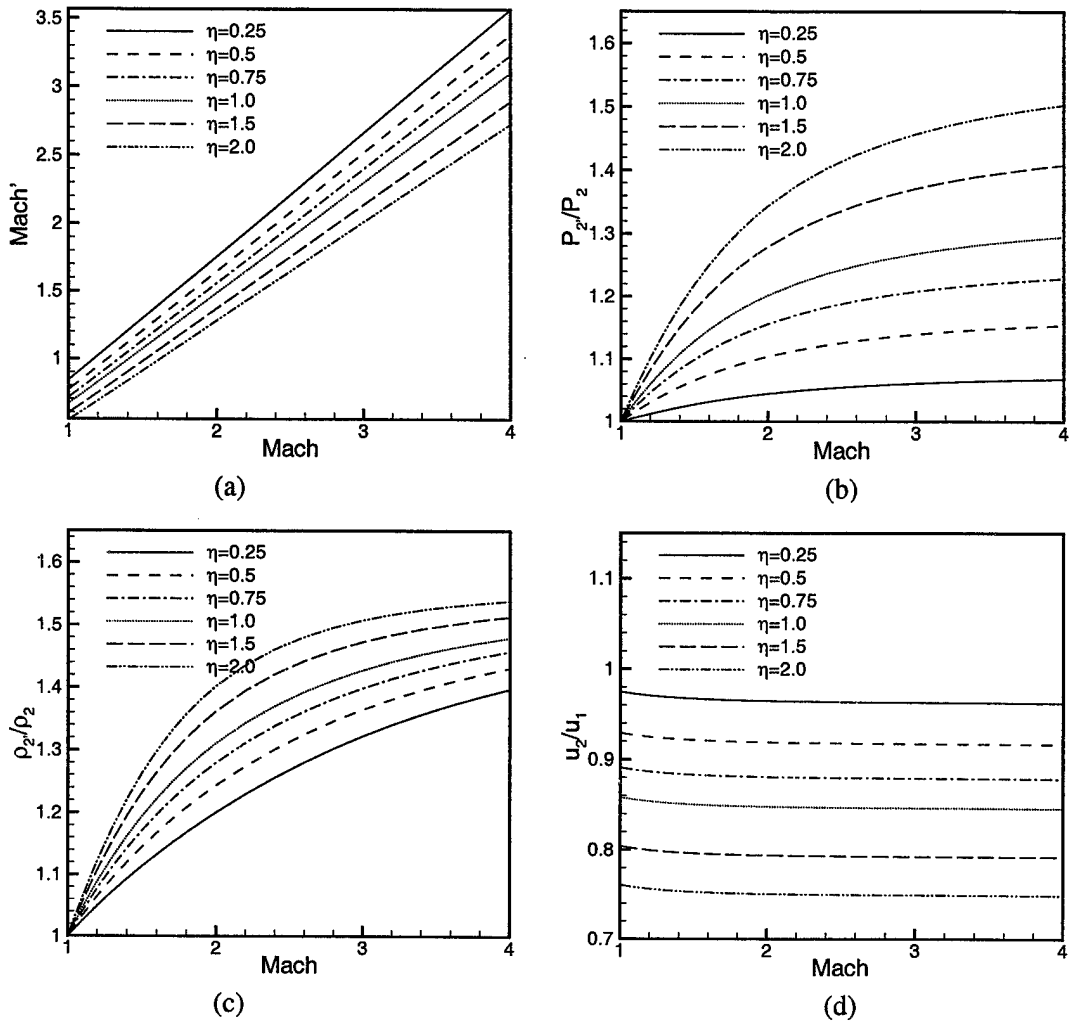

Figure 2: Mach number (a), pressure (b), density (c), and gas velocity ratios (d) are given for a shock wave impinging on a seeded gas as a function of the shock wave Mach number in unseeded gas. Assumes infinitely small glass particles with $C_s = 766$ J/kg K.

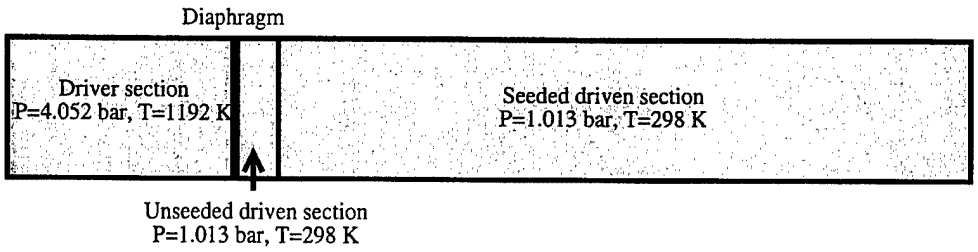

Figure 3: Schematic of experimental setup of Sommerfeld [7].

lower pressures. The device is operated by bursting the diaphragm, at which point the driver gas expands out (much like a piston), creating a shock wave that propagates through the driven gas while a rarefaction wave travels through the driver gas. The shock tube experiments that we are interested in further divide the driven section into an unseeded region and a seeded region. Of the shock tube experiments with particles and droplets, the Sommerfeld experiments [7] remain the most useful for explaining the various effects of the particle on the shock structure.

Figure 4 shows an $x - t$ diagram of a shock tube experiment with a seeded region in the driven section, as shown in Figure 3. The first event that occurs is the bursting of the diaphragm at $t = 0$. This generates a shock wave that propagates through the driven gases (S_o), and a rarefaction wave that propagates through the driver gases (R). The material interface between the driver and driven gases moves forward at a slower speed and is labeled C. Eventually the front shock wave impinges on the particle-seeded gases. Again, this results in a transmitted shock wave (S) and a reflected wave (S_r). The interface between seeded and unseeded driven gas is labeled P. The slope of the material interfaces P and C are equal, indicating both move at the same velocity ($u_{2'}$ in Figure 1).

For finite sized particles, a relaxation period occurs before the shock wave reaches an equilibrium structure where it again propagates through the medium at a constant velocity. This is different than the particle-gas equilibrium mentioned previously, because when the shock structure reaches equilibrium, not all the particles within the gas are necessarily in equilibrium with their surrounding environment. It is an equilibrium in the sense that the shock structure does not change unless it interacts with an outside force. The region after the shock wave impinges on the seeded flow but before the equilibrium shock structure is reached is called the transition region of the shock. The effect of this relaxation period on the location of the seeded-

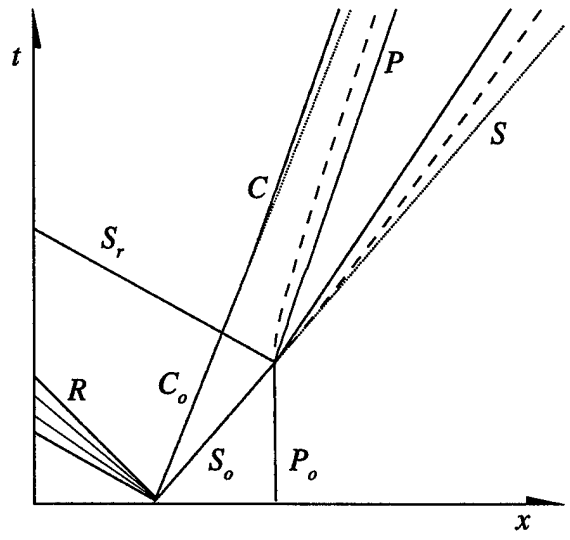

Figure 4: $x - t$ diagram of a shock tube experiment. The S_o line indicates the initial incident shock wave, S the transmitted shock, S_r is the reflected compressive waves, R is the expansion fan initiated at the diaphragm, C_o and C is the contact discontinuity separating driver and driven gases, and P is the material interface separating unseeded and seeded driven gases. The solid lines represent mitigation with infinitely-small particles, the dashed lines represent mitigation with finite-sized particles, and the dotted lines represent the unmitigated solution.

unseeded interface (P) and the front shock wave (S) are shown as dashed lines in Figure 4. Note that after this transition period, the shock wave velocity and seeded-unseeded interface velocity for finite particles approach the same velocities as for infinitely small particles, however, the material interface is displaced closer to the initial contact discontinuity.

This transition region is important to understand because it controls how far the particles penetrate into the unseeded-driven gases and whether they penetrate into the driver gases. This can considerably influence the mitigation aspects for droplets, because penetration into the high temperature driver gases will result in considerably more vaporization and reduce the force with which the driver gases are pushing the driven gases. Therefore accurately modeling this transition region is essential to give us confidence in our simulations.

In shock tubes with short driver sections and long driven sections, the rarefaction wave reflects off of the end of the tube, and then propagates toward the initial shock. When it arrives at the shock, it relieves the shock pressure, slowing down the shock wave and eventually causing the shock wave to dissipate. This

situation more closely mirrors an explosive situation, where the "driver" region (the volume of the original explosive) is very small and the rarefaction wave almost immediately begins to relieve the pressure at the shock front. For that reason, we are interested in examining cases both with long driver sections and short driver sections.

For the simulations conducted within this report, the shock tube is set up similar to the Sommerfeld experiments as is shown in Figure 3. For the experiments, the driver section was 2 m long, the unseeded driven section was 1.05 m long, and the seeded driven section was 4.76 m long. The seeded region is uniformly seeded with glass particles at a specified mass-loading. Similar geometries are also introduced to study different aspects of particle- and droplet-shock wave interactions that are not as clear with the original Sommerfeld geometry.

3 Model Development

The approach chosen for modeling sprays is the sectional Eulerian approach introduced by Tambour [9], and expanded on by Tambour [10, 11] and other researchers [12, 13]. Our research group has considerable experience with using this approach for low speed fire mitigation studies [14-17] , where it has worked quite well. Our purpose for this paper is to extend this approach for high speed flows such as found in shock tubes and blast simulations.

Lagrangian tracking of particles and droplets has been widely used to simulate these types of flows because of its flexibility and accuracy. However, to do Lagrangian tracking for individual particles is very computationally very prohibitive for large numbers of droplets. The Eulerian sectional approach provides an alternate method for doing these computations that is well suited to these problems. There are two general assumptions that make the Eulerian sectional approach attractive: first, the sprays used for mitigation are generally diffuse; that is, the number density and size of particles are small enough that the volume fraction of water is very low. Because of this, collisions between particles have a minimal influence on the dynamics of the droplets, and are ignored for this particular model. Second, although the volume fraction is fairly small, the total volume of the domain and the spray region can be quite large, thus the total number of droplets or particles can be very large. Although there has been several write-ups describing the Eulerian

sectional approach, the method is described in detail below because of differences between this approach and previous sectional approaches.

3.1 Gas-Phase Governing Equations

The governing equations for the gas-phase are the inviscid, compressible form of the conservation equations for species, mass, momentum, and energy. They are written as:

$$\frac{\partial \rho_k}{\partial t} + \nabla \cdot \rho_k \mathbf{u} = S^{m,k} \tag{4}$$

$$\frac{\partial \rho}{\partial t} + \nabla \cdot \rho \mathbf{u} = S^{m} \tag{5}$$

$$\frac{\partial \rho \mathbf{u}}{\partial t} + \nabla \cdot \rho \mathbf{u}\mathbf{u} = -\nabla P + S^{mom} \tag{6}$$

$$\frac{\partial E}{\partial t} + \nabla \cdot (E + P)\,\mathbf{u} = S^{enth} \tag{7}$$

where $S^{m,k}$, S^{m}, S^{mom}, and S^{enth} are the transfer source terms between the dispersed-phase and the gas-phase, and are explained below. Given N species, there are $N + 3$ conservation equations for the gas-phase flow in one-dimension. For the simulations completed in this report, the gas-phase is assumed to be an ideal and calorically perfect gas mixture, meaning that each species has a constant specific heat and obeys the ideal gas law. This differs from our previous report where the gas was only assumed to be thermally perfect and the specific heats were specified as functions of temperature. The relation between pressure, species densities, and temperature is given by the ideal gas law as:

$$P = R_u T \sum_{k=1}^{N} \rho_k / W_k \tag{8}$$

where R_u is the universal ideal gas constant (in molar units). Because we have a calorically perfect gas, the total internal energy is given by the relation:

$$E = \sum_{k=1}^{N} \rho_k C_{v,k} T + \frac{1}{2} \rho \mathbf{u} \cdot \mathbf{u} \tag{9}$$

The specific heat for each species is specified in terms of the specific heat ratio ($\gamma_k = C_{p,k}/C_{v,k}$) and the ideal gas constant ($R_k = R_u/W_k$) such that $C_{v,k} = R_k/(\gamma - 1)$. We use a multi-species formulation to differentiate between driver gas, driven gas, and water vapor. For air, the molecular weight is $W_{air} = 28.97$ kg/kmol and the specific heat ratio is $\gamma_{air} = 1.4$, and for water vapor the molecular weight is $W_{H_2O} = 18.015$ kg/kmol and the specific heat ratio is $\gamma_{H_2O(g)} = 1.324$.

3.2 Dispersed-Phase Governing Equations

In a very general form, the dispersed-phase can be described by a probability density function at the kinetic level. Assuming the spray is made up of spherical particles characterized by a single geometry variable ϕ (which generally is either the diameter, surface area, or volume of the droplet), single velocity $\mathbf{u}_l$, and a single temperature T_l, a probability density function $f_\phi(t, \mathbf{x}, \phi, \mathbf{u}_l, T_l)$ can be determined such that the number density at time t is given as $f_\phi \, dt \, d\mathbf{x} \, d\phi \, d\mathbf{u}_l \, dT_l$ around the point $(t, \mathbf{x}, f_\phi, \mathbf{u}_l, T_l)$. The Boltzmann kinetic transport equation for the probability density function is given by:

$$\frac{\partial f_\phi}{\partial t} + \nabla_x \cdot (\mathbf{u}_l f_\phi) + \frac{\partial}{\partial \phi}(R_\phi f_\phi) + \nabla_{u_l} \cdot (\mathbf{F} f_\phi) + \frac{\partial}{\partial T_l}(Q f_\phi) = \Gamma_c + \Gamma_e \tag{10}$$

where R_ϕ is the rate of change of the particle geometry ($R_\phi = d\phi/dt$) due to vaporization, $\mathbf{F}$ is the momentum exchange between the dispersed-phase and gas-phase, Q is the energy exchange between the dispersed-phase and gas-phase excluding phase change, Γ_c represents coalescence and break-up of the particles, and Γ_e represents elastic collisions between the particles. For this research, Γ_c and Γ_e are negligible and are not considered further. All of these functions require modeling or experiments for closure.

From this general level, one can further develop the equations in several different ways to generate usable models for simulations. The method we choose is the so-called sectional approach originally introduced by Tambour [9]. The sectional approach divides up the dispersed-phase in each cell into M discrete sections based on the size of the particles. Every section j is bounded by particle sizes $\phi^{(j)}$ and $\phi^{(j+1)}$. Our discussion of the spray model closely follows the work of Laurent and Massot [12]. Within each section, we make the following assumptions:

1. The probability density function of the spray is such that at a given size and location $(\mathbf{x}, t, \phi)$, there is

one and only one characteristic velocity and temperature.

2. The dispersion of the distribution function at a given size is zero for velocity and temperature.

3. In one section, the characteristic velocity and temperature do not depend on the size of the particles.

4. There is a one-to-one correspondence between surface temperature and particle enthalpy.

For each section, the characteristic velocity and temperature are denoted $\mathbf{u}_d$ and T_d. These assumptions allow us to express the probability density function in a much simpler form, as $n(t, \mathbf{x}, \phi)$, such that $n(t, \mathbf{x}, \phi)\, dt\, d\mathbf{x}\, d\phi$ is the probable number of particles around the point $(t, \mathbf{x}, \phi)$. We assume that the liquid or solid material is incompressible, thus the constant pressure and constant volume specific heats are equal. The specific internal energy of the particle is defined as:

$$e_d = C_l T_d + e^o_{f,l} \tag{11}$$

$e_{f,l}$ is set such that the latent heat of vaporization L_v is defined as:

$$L_v(T) = e_{H_2O(g)}(T) - e_{H_2O(l)}(T) = (C_{v,H_2O(g)} - C_l)T - e^o_{f,l} \tag{12}$$

This indicates that the latent heat of vaporization should vary with temperature, depending on the difference in constant specific heats of the vapor and liquid phases.

The basic mass, momentum, and energy equations can be recovered by multiplying Eqn. 10 by 1, $\mathbf{u}_d$, and e_d and integrating over velocity and temperature:

$$\frac{\partial n}{\partial t} + \nabla_x \cdot (n\mathbf{u}_d) + \frac{\partial}{\partial \phi}(nR_\phi) = 0 \tag{13}$$

$$\frac{\partial}{\partial t}(n\mathbf{u}_d) + \nabla_x \cdot (n\mathbf{u}_d\mathbf{u}_d) + \frac{\partial}{\partial \phi}(nR_\phi\mathbf{u}_d) = n\mathbf{F} \tag{14}$$

$$\frac{\partial}{\partial t}(ne_d) + \nabla_x \cdot (n\mathbf{u}_d e_d) + \frac{\partial}{\partial \phi}(nR_\phi e_d) = nC_l Q \tag{15}$$

For the above equations we have omitted bars associated with averaging over velocity and temperature because of the above assumptions and for clarity. To obtain the conservation equations commonly used for the sectional approach, we integrate with respect to ϕ in each section. The number density of the section is simply:

$$n^{(j)}(t,\mathbf{x}) = \int_{\phi^{(j)}}^{\phi^{(j+1)}} n(t,\mathbf{x},\phi)\, d\phi \tag{16}$$

Similarly, one can get the mass, momentum, and enthalpy densities of the dispersed-phase by integrating:

$$m^{(j)} = \int_{\phi^{(j)}}^{\phi^{(j+1)}} \rho_l V(\phi) n(t,\mathbf{x},\phi)\, d\phi \tag{17}$$

$$m^{(j)}\mathbf{u}_d^{(j)} = \int_{\phi^{(j)}}^{\phi^{(j+1)}} \rho_l V(\phi) n(t,\mathbf{x},\phi)\mathbf{u}_d(t,\mathbf{x})\, d\phi \tag{18}$$

$$m^{(j)}e_d^{(j)} = \int_{\phi^{(j)}}^{\phi^{(j+1)}} \rho_l V(\phi) n(t,\mathbf{x},\phi)e_d(t,\mathbf{x})\, d\phi \tag{19}$$

where ρ_l is the density and $V(\phi)$ is the volume of the particles. Other terms in the overall conservation equations are similarly treated:

$$m^{(j)}\mathbf{F}^{(j)} = \int_{\phi^{(j)}}^{\phi^{(j+1)}} \rho_l V(\phi) n(t,\mathbf{x},\phi)\mathbf{F}(t,\mathbf{x},\phi)\, d\phi \tag{20}$$

$$m^{(j)}Q^{(j)} = \int_{\phi^{(j)}}^{\phi^{(j+1)}} \rho_l V(\phi) n(t,\mathbf{x},\phi)C_l Q(t,\mathbf{x},\phi)\, d\phi \tag{21}$$

$$m^{(j)}R_\phi^{(j)} = \int_{\phi^{(j)}}^{\phi^{(j+1)}} \rho_l V(\phi)\frac{\partial}{\partial\phi}\left[n(t,\mathbf{x},\phi)R_\phi(t,\mathbf{x},\phi)\right]\, d\phi \tag{22}$$

Integration by parts is used for Eqn. 22 to obtain a more convenient representation of the vaporization:

$$\int_{\phi^{(j)}}^{\phi^{(j+1)}} \rho_l V\frac{\partial}{\partial\phi}\left(nR_\phi\right)\, d\phi = \rho_l nR_\phi V|_{\phi^{(j)}}^{\phi^{(j+1)}} - \int_{\phi^{(j)}}^{\phi^{(j+1)}} \rho_l nR_\phi\frac{dV}{d\phi}\, d\phi \tag{23}$$

This allows us to define two vaporization terms, given below:

$$E_1^{(j)} = -\rho_l n(t,\mathbf{x},\phi^{(j)})R_\phi(\phi^{(j)})V(\phi^{(j)}) \tag{24}$$

$$E_2^{(j)} = -\int_{\phi^{(j)}}^{\phi^{(j+1)}} \rho_l nR_\phi\frac{dV}{d\phi}d\phi \tag{25}$$

Physically, $E_1^{(j)}$ represents transport of mass from section j to section $(j-1)$, and $E_2^{(j)}$ represents transport of mass from section j to the gas-phase.

The conservation equations are then written for each section j in the typical sectional form:

$$\frac{\partial m^{(j)}}{\partial t} + \nabla_x \cdot \left(m^{(j)} \mathbf{u}_d^{(j)} \right) = - \left(E_1^{(j)} + E_2^{(j)} \right) m^{(j)} + E_1^{(j+1)} m^{(j+1)} \tag{26}$$

$$\frac{\partial}{\partial t} \left(m^{(j)} \mathbf{u}_d^{(j)} \right) + \nabla_x \cdot \left(m^{(j)} \mathbf{u}_d^{(j)} \mathbf{u}_d^{(j)} \right) = - \left(E_1^{(j)} + E_2^{(j)} \right) m^{(j)} \mathbf{u}_d^{(j)} + E_1^{(j+1)} m^{(j+1)} \mathbf{u}_d^{(j+1)} + m^{(j)} \mathbf{F}^{(j)} \tag{27}$$

$$\begin{aligned} \frac{\partial}{\partial t} \left(m^{(j)} e_d^{(j)} \right) + \nabla_x \cdot \left(m^{(j)} e_d^{(j)} \mathbf{u}_d^{(j)} \right) &= - \left(E_1^{(j)} + E_2^{(j)} \right) m^{(j)} e_d^{(j)} + E_1^{(j+1)} m^{(j+1)} e_d^{(j+1)} \\ &+ m^{(j)} \left(Q^{(j)} - E_2^{(j)} L_v \right) + m^{(j)} \mathbf{F}^{(j)} \cdot \mathbf{u}_d^{(j)} \end{aligned} \tag{28}$$

The source terms for the gas-phase are simply:

$$S^m = - \sum_{j=1}^{M} E_2^{(j)} m^{(j)} \tag{29}$$

$$S^{mom} = - \sum_{j=1}^{M} \left(E_2^{(j)} m^{(j)} \mathbf{u}_d^{(j)} - \mathbf{F}^{(j)} m^{(j)} \right) \tag{30}$$

$$S^{enth} = - \sum_{j=1}^{M} \left(E_2^{(j)} m^{(j)} e_d^{(j)} - m^{(j)} \left(Q^{(j)} - E_2^{(j)} L_v \right) - m^{(j)} \mathbf{F}^{(j)} \cdot \mathbf{u}_d^{(j)} \right) \tag{31}$$

The species source term is simply the mass source term for the water vapor species, and zero for everything else.

3.3 Particle/Droplet Models

To develop expressions for $E_1^{(j)}$, $E_2^{(j)}$, $\mathbf{F}^{(j)}$, and $Q^{(j)}$ we need to use particle and droplet models to represent the processes of vaporization, heat transfer, and drag. The present simulations use models that have been used widely in the droplet community. We describe these models briefly below. The models are based on drag and vaporization around a single particle in quiescent flow, that are then corrected for different flow regimes based on empirical correlations.

Particle drag is computed based on Stokes flow with high velocity correction terms [18]. For a single particle,

$$\rho_l V \frac{d\mathbf{u}_d}{dt} = 3\pi\mu \mathbf{u}_r D(1 + 0.15 Re^{0.687}) \tag{32}$$

where μ is the gas viscosity at the particle temperature. We use this expression to obtain an expression for $\mathbf{F}$ found in Eqn. 10:

$$\mathbf{F} = \frac{3\pi\mu}{\rho_l V} \mathbf{u}_r D(1 + 0.15 Re^{0.687}) \tag{33}$$

The evolution of the temperature of the particle is given as

$$\rho_l V C_l \frac{dT_d}{dt} = \pi D^2 h[T - T_d] + \rho_l \frac{dV}{dt} L_v \tag{34}$$

where $h = Nu\lambda/D$ is the heat transfer coefficient, T is the far-field gas temperature, L_v is the latent heat of vaporization, T_d is the particle temperature, and Nu is the Nusselt number. The Q in Eqn. 10 is the heat transfer from the gas phase into the liquid phase, and does not account for phase change, thus

$$Q = \frac{\pi D^2 h}{\rho_l V C_l}[T - T_d] \tag{35}$$

The Nusselt number can either be assumed to be 2 (appropriate for non-convective environments), or for convective environments it can be represented by the formula:

$$Nu = 2 + 0.459 Pr^{1/3} Re^{0.55} \tag{36}$$

The vaporization models used for all of the water droplet simulations in this report are based on spherically-symmetric isolated droplet solutions, with modifications added based on experimental correlations to account for convective effects. The first model we use is the basic D^2-law given by:

$$\frac{d}{dt} D^2 = -\beta \tag{37}$$

where D is the particle diameter and β is the vaporization coefficient. The model used assumes a simple temperature dependent expression for the vaporization such that:

$$\beta(T) = \beta_0 \left[1 + 7.4233 \times 10^{-7} \left(T - 300\right)^{2.7548}\right] \tag{38}$$

where $\beta_0 = 7600\ \mu\text{m}^2/\text{s}$, obtained from [19, 20]. This will be referred to as the empirical-β model, because it is based totally on empirical data. Although a simple and efficient model, a significant problem with this model is that it does not account for droplet heat-up. For our simulations, as the shock wave passes a given droplet, initially the droplet vaporization will be small as most of the available heat is used to heat up the droplet to near its boiling point. Only after the droplet is heated somewhat will vaporization become significant. This heat-up period is critical, since to be effective the droplet must vaporize close to the shock wave.

The second vaporization model addresses this issue. It is based on the classical spherically-symmetric droplet vaporization model of Spalding [21, 22], but includes effects from droplet heating. The model assumes the gaseous-H_2O pressure at the surface of the droplet is the equilibrium vapor pressure of water at the local temperature, and is thus called the equilibrium model throughout this report. Note that this is yet another equilibrium that only pertains to the amount of water vapor at the droplet surface. It is not in any way associated with the gas-particle equilibrium or the shock structure equilibrium mentioned previously. Assuming a unity Lewis number, the vaporization coefficient β is calculated as:

$$\beta = \frac{8\lambda}{\rho_l C_p} \ln(B+1) \tag{39}$$

where λ is the thermal conductivity of the gas, ρ_l is the liquid density, C_p is the constant pressure specific heat of the gas, and B is the Spalding transfer number, defined as:

$$B = (Y_{H_2O,g} - Y_{H_2O,s})/(Y_{H_2O,s} - 1) \tag{40}$$

where $Y_{H_2O,g}$ is the mass fraction of water in the far-field, $Y_{H_2O,s}$ is the mass fraction of water at the surface of the droplet. $Y_{H_2O,s}$ is calculated from the partial pressure of water at the droplet surface,

$$Y_{H_2O,s} = \frac{P_{H_2O,sat}(T_d) W_{H_2O}}{PW} \tag{41}$$

where $P_{H_2O,sat}$ is the saturation pressure of water, T_d is the droplet temperature, W_{H_2O} is the molecular weight of water, and W is the molecular weight of the gas mixture.

Assuming the D^2-law, the spherically-symmetric mass vaporization rate for a single droplet is calculated as:

$$\dot{m}_{ss} = \rho_l \frac{dV}{dt} = \rho_l \frac{\pi D}{4} \frac{dD^2}{dt} = -\rho_l \frac{\pi D \beta}{4} \tag{42}$$

where $\dot{m}_{ss}$ represents the spherically symmetric solution. For convective environments, the correlation of Ranz and Marshall [23] can be used to determine the correct vaporization rate. This is expressed as:

$$\dot{m} = \dot{m}_{ss} \left[1 + 0.3 Pr^{1/3} (2Re^{1/2})\right] \tag{43}$$

where V is the droplet volume, $Pr = \mu C_p/\lambda$ is the gas-phase Prandtl number at the droplet temperature, and $Re = \rho u_r D/\mu$ is the Reynolds number based on droplet diameter, gas density and viscosity, and relative velocity $u_r = |\mathbf{u}_r| = |\mathbf{u} - \mathbf{u}_d|$. Note that all unsubscripted variables are gas quantities.

For the vaporization models, the heat transfer is modified by an additional term that is typically expressed in the Nusselt Number:

$$Nu = Nu^* \left[\frac{\ln(1+B)}{B}\right] \tag{44}$$

where Nu^* is the original Nusselt number for non-vaporizing particles expressed in Eqn. 36. The additional term does not change the expressions developed for the sectional source terms, as the additional term is independent of droplet geometry.

For the drag and heat transfer computations, the Sutherland expression is used for expressing viscosity as a function of temperature in air:

$$\mu(T) = \mu_{ref}\left(\frac{T^{3/2}}{110+T}\right) \tag{45}$$

where $\mu_{ref} = 1.458\times10^{-6}$ kg/(m sec) for a mixture containing predominantly air. The thermal conductivity is calculated assuming a constant Prandtl number of 0.75,

$$\lambda(T) = \frac{\mu(T)C_p}{Pr} \tag{46}$$

For glass particles, the only physical properties we need are the density of glass $\rho_{glass} = 2500$ kg/m^3 and the constant specific heat for glass $C_{glass} = 766$ J/kg K. For liquid water droplets has a constant density of $\rho_{H_2O(l)} = 1000$ kg/m^3 and a constant specific heat of $C_{H_2O(l)} = 4184$ J/kg K. The latent heat of vaporization is $L_v = 2.3049 \times 10^6$ J/kg at 300 K. The saturation pressure of water $P_{H_2O,sat}(T)$ is curve fit with widely available data and has a form similar to the Clausius-Clapeyron equation:

$$P_{H_2O,sat}(T) = A\exp\left(-\frac{B}{T+C}\right) \tag{47}$$

where for water, $A = 1.20967 \times 10^5$ bar, $B = 3835.83$ K, and $C = -45$ K. As with the glass particles, we use the Sutherland expressions to determine the viscosity and thermal conductivity as a functions of the temperature only (Eqns. 45 and 46).

For the simulations, a cutoff temperature is arbitrarily chosen below which the vaporization rate becomes zero. This temperature is selected above 300 K such that no vaporization takes place before the shock wave reaches the droplets. For these simulations, a value of $T_c = 310$ K was chosen. Lower values between 300 and 310 K could also be chosen, but only have a minor effect on the solutions.

3.4 Cross-coupling Source Terms for the Eulerian Sectional Approach

Given models that describe single-particle behavior, we develop expressions for the source terms found in the sectional conservation Eqns. 26-29. For the model development, we choose the geometry variable ϕ to be the volume V. An important point to mention is that the resulting source terms are different depending on whether ϕ represents the diameter D, surface area S, or volume V. In the work of Greenberg and Tambour[23], they choose V as their geometric variable, however, Laurent and Massot[12] have chosen the surface area S as their geometric variable.

The fundamental approximation of the sectional approach assumes a relationship between the number probability density function $n(t, \mathbf{x}, \phi)$ and the geometry variable ϕ within each section. The most reasonable choice is to take $n(t, \mathbf{x}, \phi)$ to be a constant ($\kappa^{(j)}$) in each section. This simplifies the resulting integration and gives a clear method of refinement. Either the number density or the mass density formulas can be used to fix the value of $n(t, \mathbf{x}, \phi) = \kappa^{(j)}$ for section j. We find that fixing it with respect to the mass density is the most convenient.

Both the surface area S and the particle diameter D can be related to the particle volume V through:

$$D = \sqrt[3]{\frac{6V}{\pi}} \tag{48}$$

$$S = \sqrt[3]{\pi}\,(6V)^{2/3} \tag{49}$$

The first step is to determine the value for $\kappa^{(j)}$ for each section. This is done by using the definition of mass density for the section, Eqn. 17.

$$m^{(j)} = \int_{V^{(j)}}^{V^{(j+1)}} \rho_l V n(t, \mathbf{x}, V)\, dV \tag{50}$$

Noting that $n = \kappa^{(j)}$ and is a constant with respect to V, this equation is integrated to get

$$m^{(j)} = \frac{1}{2}\rho_l \kappa^{(j)} \left[(V^{(j+1)})^2 - (V^{(j)})^2\right] \tag{51}$$

solving for $\kappa^{(j)}$ we get

$$\kappa^{(j)} = \frac{2m^{(j)}/\rho_l}{(V^{(j+1)})^2 - (V^{(j)})^2} \tag{52}$$

For calculating the vaporization rate terms $E_1^{(j)}$ and $E_2^{(j)}$, we develop an expression for $R_\phi = dV/dt$ based on the D^2-law (Eqn. 37). Knowing that $V = (\pi/6)D^3$ and through differentiation and algebraic manipulation of the D^2-law, we obtain an expression for the change in volume for the spherically symmetric droplet:

$$\frac{dV_{ss}}{dt} = -\frac{1}{4}\sqrt[3]{6\pi^2}V^{1/3}\beta \tag{53}$$

Using the droplet vaporization correlation of Ranz and Marshall (Eqn. 43), we obtain the change in volume for the droplet in a convective environment as:

$$R_\phi = \frac{dV}{dt} = \frac{dV_{ss}}{dt}\left[1 + 0.3Pr^{1/3}(2Re^{1/2})\right] = -\frac{1}{4}\sqrt[3]{6\pi^2}V^{1/3}\beta\left[1 + 0.3Pr^{1/3}(2Re^{1/2})\right] \tag{54}$$

Pulling the droplet diameter out of the Reynolds number, substituting this and the value for $\kappa^{(j)}$ into Eqn. 24 we get an expression for $E_1^{(j)}$ as

$$E_1^{(j)} = \sqrt[3]{\frac{3\pi^2}{4}}\frac{m^{(j)}\beta}{(V^{(j+1)})^2 - (V^{(j)})^2}\left[(V^{(j)})^{4/3} + A(V^{(j)})^{3/2}\right] \tag{55}$$

where $A = 0.3(6/\pi)^{1/6}Pr^{1/3}(2\rho u_r/\mu)^{1/2}$. By a similar means, we substitute into the definition for $E_2^{(j)}$ to obtain the integral:

$$E_2^{(j)} = \int_{V^{(j)}}^{V^{(j+1)}} \rho_l \kappa^{(j)}\left[\frac{1}{4}\sqrt[3]{6\pi^2}V^{1/3}\beta\right]\left[1 + 0.3Pr^{1/3}(2Re^{1/2})\right]dV \tag{56}$$

Integrating this and evaluating the result at $V^{(j+1)}$ and $V^{(j)}$, we obtain:

$$E_2^{(j)} = \sqrt[3]{\frac{3\pi^2}{4}}\left[\frac{m^{(j)}\beta}{(V^{(j+1)})^2 - (V^{(j)})^2}\right]\left\{\frac{3}{4}\left[(V^{(j+1)})^{4/3} - (V^{(j)})^{4/3}\right] + \frac{2}{3}A\left[(V^{(j+1)})^{3/2} - (V^{(j)})^{3/2}\right]\right\} \tag{57}$$

Using the particle drag model (Eqn. 32), we develop an equation for the integrated force felt on section j as defined in Eqn. 20. The function $\mathbf{F}$ found in Eqn. 20 is the acceleration felt by a particle due to drag, and is thus:

$$\mathbf{F}(V) = \frac{3\pi\mu\mathbf{u}_r}{\rho_l V}\sqrt[3]{\frac{6V}{\pi}}\left[1 + 0.15\left(\frac{Re}{D}\right)^{0.687}\left(\frac{6V}{\pi}\right)^{0.229}\right] \tag{58}$$

To solve for the cumulative force, we take Eqn. 20 and substitute the above expression in for $\mathbf{F}$, substitute $\kappa^{(j)}$ for n, and substitute V for $D = \sqrt[3]{6V/\pi}$ to get

$$m^{(j)}\mathbf{F}^{(j)} = \int_{V^{(j)}}^{V^{(j+1)}} 3\kappa^{(j)}\pi\mu\mathbf{u}_r\left[\sqrt[3]{\frac{6V}{\pi}} + 0.15\left(\frac{Re}{D}\right)^{0.687}\left(\frac{6V}{\pi}\right)^{0.5623}\right]dV \tag{59}$$

This term is then split into two terms, $\mathbf{F}_1^{(j)}$ and $\mathbf{F}_2^{(j)}$, for simplicity. Integration of the $\mathbf{F}_1^{(j)}$ equation with respect to V is easily done, and with some rearrangement and substitution of $\kappa^{(j)}$, we get the following expression:

$$m^{(j)}\mathbf{F}_1^{(j)} = m^{(j)}\frac{9}{\rho_l}\sqrt[3]{\frac{3\pi^2}{4}}\left[\frac{(V^{(j+1)})^{4/3} - (V^{(j)})^{4/3}}{(V^{(j+1)})^2 - (V^{(j)})^2}\right]\mu\mathbf{u}_r \tag{60}$$

Determination of the $\mathbf{F}_2^{(j)}$ is also simple, although the algebra is a bit messier. First, we substitute in for the Reynolds number $Re/D = \rho u_r/\mu$, and integrate with respect to volume:

$$m^{(j)}\mathbf{F}_2^{(j)} = \frac{0.45\pi}{1.5623}\left(\frac{6}{\pi}\right)^{0.5623}\kappa^{(j)}\left[(V^{(j+1)})^{1.5623} - (V^{(j)})^{1.5623}\right]\left(\frac{\rho u_r}{\mu}\right)^{0.687}\mu\mathbf{u}_r \tag{61}$$

substituting in for $\kappa^{(j)}$ and multiplying out the initial numbers we get the expression:

$$m^{(j)}\mathbf{F}_2^{(j)} = m^{(j)}\frac{2.604}{\rho_l}\left[\frac{(V^{(j+1)})^{1.5623} - (V^{(j)})^{1.5623}}{(V^{(j+1)})^2 - (V^{(j)})^2}\right]\left(\frac{\rho u_r}{\mu}\right)^{0.687}\mu\mathbf{u}_r \tag{62}$$

The last expression we need is for $m^{(j)}Q^{(j)}$. For this, we need an expression for Q, the change in temperature with respect to time. An equation is developed from Eqn. 34 as:

$$Q = \frac{\pi D^2 h T_r}{4\rho_l V C_l} = \frac{\pi D\lambda T_r}{4\rho_l V C_l}\left[2 + 0.459Pr^{1/3}Re^{0.55}\right] \tag{63}$$

Expressing this in terms of the volume of the particle V,

$$Q(V) = \frac{\pi\lambda T_r}{4\rho_l V C_l}\sqrt[3]{\frac{6V}{\pi}}\left[2 + 0.459Pr^{1/3}\left(\frac{\rho u_r}{\mu}\right)^{0.55}\left(\frac{6V}{\pi}\right)^{0.183}\right] \tag{64}$$

This expression is also split this into two terms, $Q_1^{(j)}$ and $Q_2^{(j)}$ to simplify the integrals:

$$m^{(j)}Q_1^{(j)} = \int_{V^{(j)}}^{V^{(j+1)}}\kappa^{(j)}\frac{\sqrt[3]{6\pi^2}}{2C_l}\lambda T_r V^{1/3}dV \tag{65}$$

Doing the integration, and substituting in for $\kappa^{(j)}$,

$$m^{(j)}Q_1^{(j)} = m^{(j)}\frac{3\sqrt[3]{6\pi^2}}{4C_l\rho_l}\left[\frac{(V^{(j+1)})^{4/3} - (V^{(j)})^{4/3}}{(V^{(j+1)})^2 - (V^{(j)})^2}\right]\lambda T_r \tag{66}$$

The second term can be obtained similarly,

$$m^{(j)}Q_2^{(j)} = \int_{V^{(j)}}^{V^{(j+1)}}\kappa^{(j)}\frac{0.1148\pi}{C_l}\left(\frac{6}{\pi}\right)^{0.5167}Pr^{1/3}\left(\frac{\rho u_r}{\mu}\right)^{0.55}\lambda T_r V^{0.5167}dV \tag{67}$$

Again, by integrating and substituting into $\kappa^{(j)}$ we obtain a more manageable expression:

$$m^{(j)}Q_2^{(j)} = m^{(j)}\frac{0.6635}{\rho_l C_l}Pr^{1/3}\left(\frac{\rho u_r}{\mu}\right)^{0.55}\left[\frac{(V^{(j+1)})^{1.5167} - (V^{(j)})^{1.5167}}{(V^{(j+1)})^2 - (V^{(j)})^2}\right]\lambda T_r \tag{68}$$

The above expressions for $E_1^{(j)}$, $E_2^{(j)}$, $\mathbf{F}^{(j)}$, and $Q^{(j)}$ close the system of conservation Eqns. 26 -29, and allows us to solve the system of equations.

4 Solution Procedure

The solution procedure involves solving $M + 1$ sets of conservation equations, where M is the number of sections being simulated. Each set contains a continuity equation, momentum equations, and an energy equation. The sets are coupled together through the source terms described above. The present procedure used for solving these conservation equations is by a time-step splitting method. Each set of conservation equations is solved independently without the cross-coupling source terms. Because the gas-phase and dispersed-phase can have significantly different time-step restrictions, the gas-phase solution is allowed to take several time-steps for each dispersed-phase time-step taken. The cross-coupling source terms are added at the end of each dispersed-phase time-step.

4.1 Gas-phase solution procedure

The solution procedure used for the gas-phase conservation Eqns. 5-7 is the FCT-algorithm of Boris and Book [24], which is especially well suited for high-speed flows. The version of the algorithm used in this project is described in detail in NRL/MR/6410-93-7192 [25], and will not be repeated here for brevity. Unlike the computations described in the memorandum report, we use the explicit ideal gas law (Eqn. 8) and the energy definition (Eqn. 9) instead of combining the two to obtain an expression for pressure based on internal energy.

4.2 Dispersed-phase solution procedure

The solution procedure used for the dispersed-phase conservation Eqns. 26-29, is also based on the explicit-FCT algorithm used above. Examining the conservation equations, notice that the momentum equation is decoupled from the energy equation. One benefit of this is that the Courant number restriction for the

numerical procedure is based on the particle velocity ($\mathbf{u}_d^{(j)}$) instead of the acoustic velocities as for the gas-phase, allowing for much larger time-steps. The internal energy and the temperature of the dispersed-phase is similarly related through a constant specific heat ($e_d^{(j)} = C_l T_d^{(j)} + e_{f,l}^o$).

4.3 Gas/dispersed-phase coupling

The gas/dispersed-phase coupling terms are only added to the solution after each particle-section advances one time-step, and the gas-phase has advanced multiple time-steps. The coupling terms are then added explicitly. Each section of the dispersed-phase is coupled to the neighboring sections through the vaporization term $E_1^{(j)}$ (Eqn. 24). Every section is coupled to the gas-phase through the second vaporization term $E_2^{(j)}$ (Eqn. 25), the momentum transfer term $\mathbf{F}^{(j)}$ (Eqn. 20), and the heat transfer term $Q^{(j)}$ (Eqn. 21). For our selection of $\phi = V$ and with the droplet/particle models presented above, the final expression for $E_1^{(j)}$ is given in Eqn. 55, $E_2^{(j)}$ is given in Eqn. 57, the drag source term $\mathbf{F}^{(j)}$ is given in Eqns. 60 and 62, and the heat transfer source term $Q^{(j)}$ is given in Eqns. 66 and 68. The complete source terms introduced to the gas-phase conservation equations are given in Eqns. 29-31.

4.4 Initial and Boundary Conditions

The simulations for this report are all one-dimensional shock tube simulations. The basic geometry is shown in Figure 3. The solution domain is divided into three sections: a driver section, an unseeded driven section, and a seeded driven section. In each section the temperature, pressure, and composition are uniform initially. The seeded region contains uniformly distributed particles at a specified mass-loading. The velocity for the entire domain is initially zero, and the particles are assumed to be perfectly suspended in the gas with zero velocity. This type of simulation is equivalent to experiments involving shock tubes with diaphragms, where a diaphragm initially separates the driver and driven gases and is burst at the start of the experiment. The driver gas is at a much higher pressure, and thus pushes the driven gases much like a piston, creating a shock that propagates through the driven gases.

Boundary conditions for each end of the shock tube are perfectly reflecting walls. Typically, the simulation is stopped before the shock wave reflects off of the right wall. The rarefaction waves do, however, reflect off of the left wall and can subsequently influence the shock wave.

5 Numerical Model Validation

Numerical validation of the computational scheme used the exact Sommerfeld geometry [7], consisting of a 2 m long driver section, a 1.05 m long unseeded driven section, and a 4.76 m long seeded driven section. The driven section was seeded with mono-dispersed 27 μm glass particles. Several experiments were run with varying amounts of mass-loading, and with different driver pressures. The driver section pressures are indicated below for each case. The resolution of the simulation is approximately 2.5 mm per cell, enough to obtain accurate solutions, but it does cause some noise in the shock wave Mach number calculation.

Sommerfeld was interested primarily in the transition region between a shock wave traveling through unseeded flow and seeded flow, as is shown in Figure 4. In the transition region, the shock wave decelerates from the unseeded shock wave velocity to the equilibrium shock wave velocity in the seeded mixture. Because the energy and momentum transfer are not instantaneous between the gas and dispersed-phase, the shape of the pressure and temperature profiles behind the shock wave also changes due to the particles. To ensure the expansion fan did not reflect back and impact the front shock, he used a fairly long driver section (which is typical of many shock tube experiments). In addition, Sommerfeld used a fairly large unseeded driven section to ensure that the shock wave was properly formed before impacting the seeded gas.

In Figure 5, we show comparisons of shock wave Mach number between four separate Sommerfeld experiments and their corresponding simulations. The comparison for all four cases is fairly good. The experimental results (shown as symbols on each of the four plots), shows that the transition region can be very roughly divided into three almost linear segments. Initially, the deceleration is very fast. At about one meter past the seeded-unseeded interface, the deceleration abruptly slows. At about three meters past the interface, the deceleration again slows as it approaches the shock structure equilibrium value for the gas-particle mixture (found from the equivalent-gas analysis presented earlier).

For the simulations, the initial deceleration is accurately captured for all cases. The abrupt change in the deceleration is not totally caught in all the numerical simulations, resulting in slightly lower Mach numbers in the calculations as compared to the experiments for the Mach number 1.49 and 1.26 cases with mass-loading of 0.63. Interestingly, the higher mass-loading cases and higher velocity cases capture this shift in deceleration fairly accurately, and do not show the same type of errors. The poorest comparison is with the

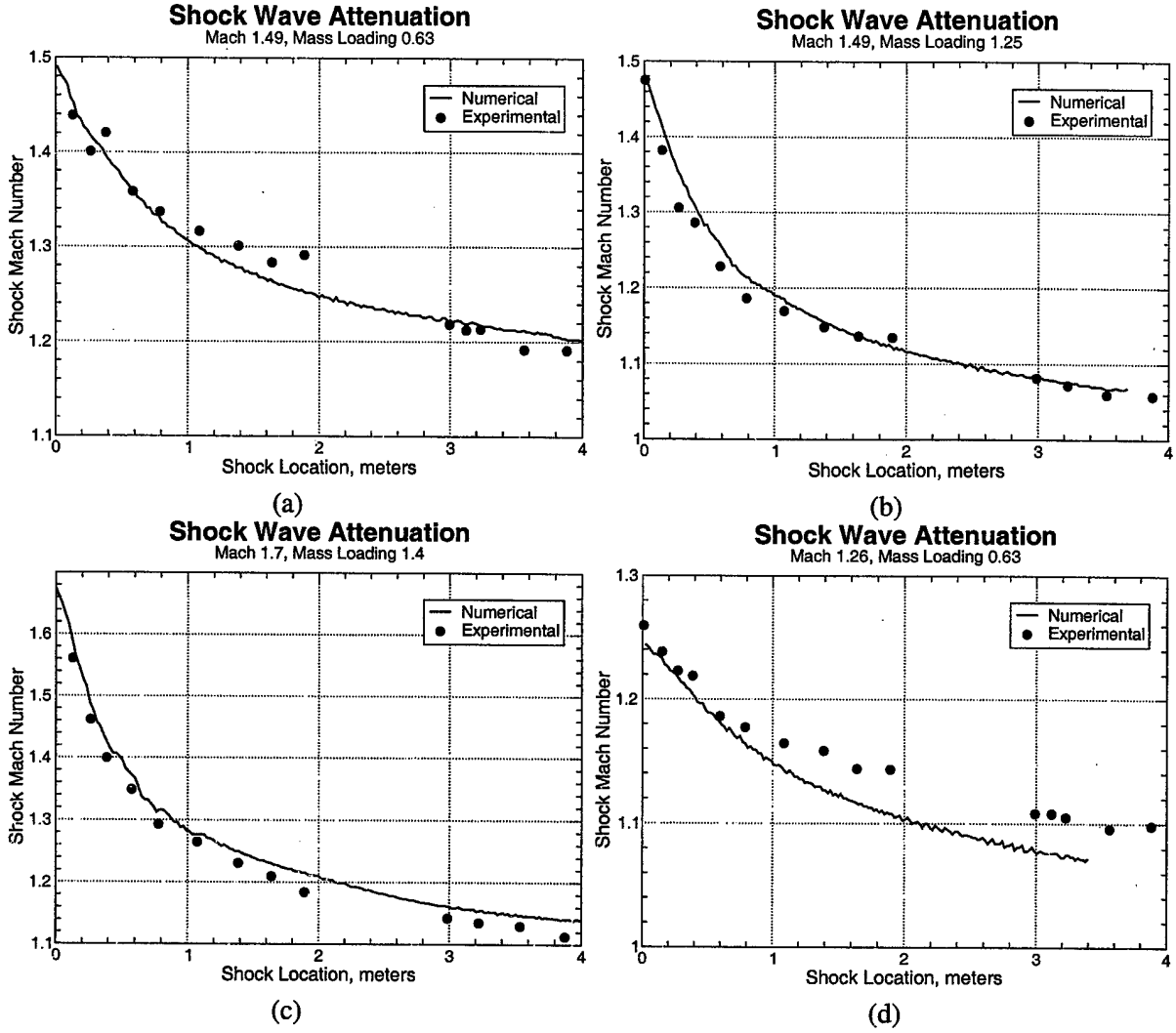

Figure 5: Comparison between numerical simulations and experiments [7] for shock wave Mach numbers. The air is seeded with 27 μm glass particles with the given mass-loading.

low Mach number case (Fig. 5d), although there is no clear reason why this discrepancy should exist for this case. Our results are consistent with other numerical simulations of the Sommerfeld simulations, presented by Sommerfeld and other researchers, indicating that the problem is either with the underlying model for low Mach number shock waves or with the experiment itself, and not with our implementation of the model.

The effect of including particle heating in the model is shown clearly in Figure 6. Within two meters of the start of the seeded section, the simulation results are very close, with the simulation without particle heating actually comparing slightly better with experiments than the simulations with particle heating. Further downstream, however, the case without particle heating underpredicts the attenuation. This is because

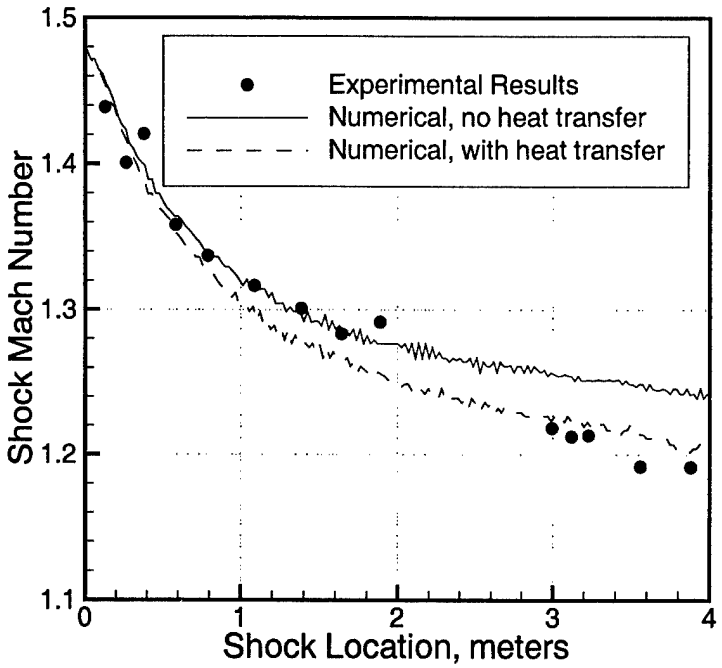

Figure 6: Effect of particle heating on shock wave Mach number. $M_o = 1.49$, $\eta = 0.63$, 26-28 μm glass particles.

of the additional energy that is taken out of the gas flow to equilibrate the temperatures for the simulations with particle heating. This energy is never removed for the case without particle heating, resulting in an incorrect "equilibrium" shock wave Mach number.

A possible reason for the better comparison early in the transition region for the simulation without heat transfer could be because of the infinite conductivity model used for the particle heating. This model keeps the surface temperature of the particles artificially low, increasing the heat transfer and decelerating the shock wave prematurely. As the particles start to equilibrate, the infinite conductivity model becomes a better approximation, and the experimental and numerical results start to show better agreement. One of the limitations of the sectional approach is the necessity of using an infinite conductivity approach, instead of more complex temperature models for the droplets. This issue also appears when discussing the equilibrium vaporization model below.

In the original Sommerfeld paper, the experimental procedure for producing a pressure ratio of four between the driver and driven gas is not specified. In all the simulations to this point, an assumption was made that the pressure was raised through heating the driver gas (and having the density remain constant).

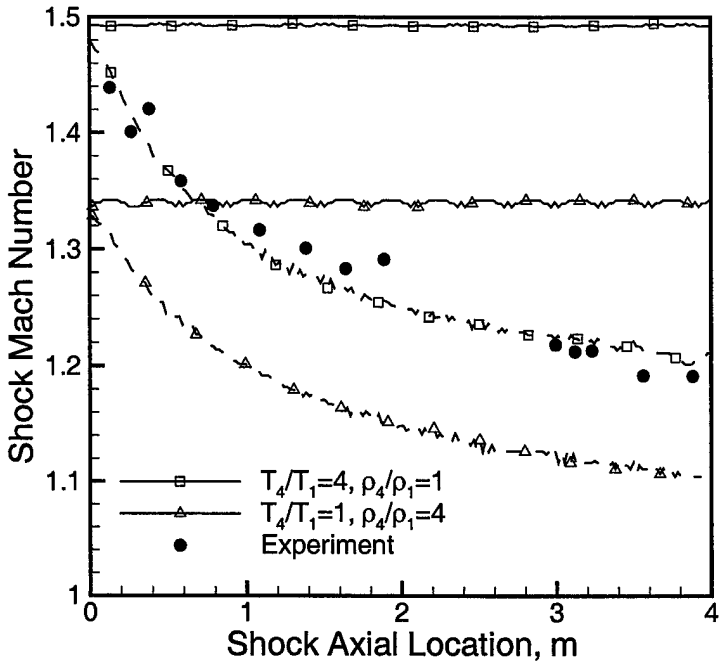

Figure 7: Comparison of unmitigated and mitigated shock wave Mach numbers. The initial pressure difference for the shock tubes is obtained through temperature ($T_4/T_1 = 4$, $\rho_4/\rho_1 = 1$) or density ($\rho_4/\rho_1 = 4$, $T_4/T_1 = 1$). $P_4/P_1 = 4$, $\eta = 0.63$, 26-28 μm glass particles.

Another procedure to obtain an initial pressure ratio of four is to compress the gas and keep the temperature constant. These two different initial conditions are compared below in Figures 7 and 8 with (dashed) and without (solid) particle seeding. There is considerable difference between the solutions due to the initial conditions, although the transition behavior is very similar between the two cases. From the results above it is apparent that Sommerfeld used heating to obtain the correct pressure difference between the driver and driven gases. However, we present both results for completeness, and note that most shock tubes generally use a combination of heating and compression to obtain the desired pressure difference between driver and driven gases.

Some insight into the reasons for the difference are apparent from examining pressure profiles as shown in Figure 8. The left side corresponds to an initial driver temperature ratio of $T_4/T_1 = 1$ and a density ratio of $\rho_4/\rho_1 = 4$, and the right side corresponds to the inverse ($T_4/T_1 = 4$, $\rho_4/\rho_1 = 1$). Note that the second case is simply the validation case presented above in Figure 5b. Although both simulations used the same driver pressure, the shock pressure that develops for each case is significantly different, resulting in the different shock wave Mach numbers observed in Figure 7. The dashed lines show computations with

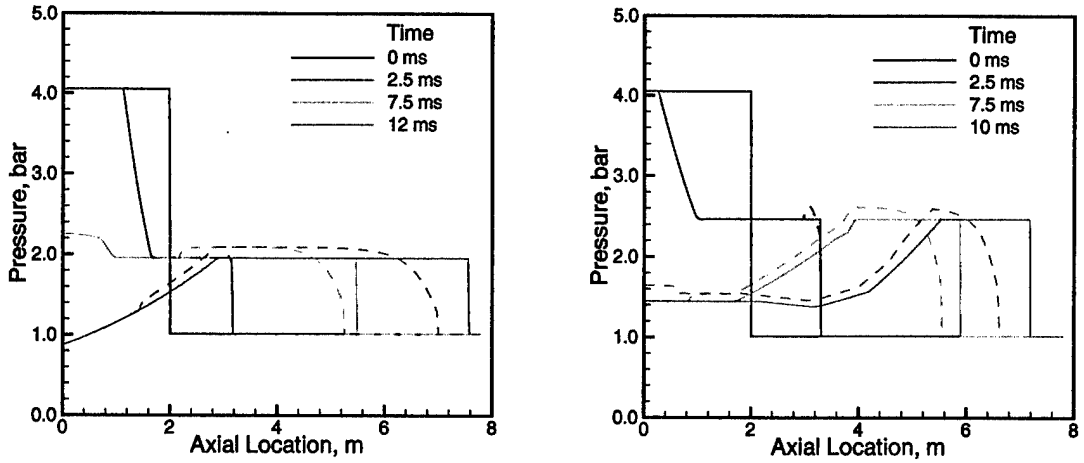

Figure 8: Snapshot of solutions for unmitigated (solid) and mitigated (dashed) shocks. The initial pressure difference for the shock tube is obtained through temperature (a) or density (b). $P_4/P_1 = 4$, $\eta = 0.63$, 26-28 μm glass particles.

particle-seeding of the flow, and clearly show that in both cases the shock wave slows down after it enters the seeded region.

The Sommerfeld experiments (and many other experiments) focused on the shock wave Mach number in the transition region of the flow-field. Although this is an important aspect of mitigation, also of interest is the shock overpressure and maximum overpressure felt at any given point in the domain. While for unseeded shocks (and shocks seeded with infinitely small particles), shock overpressure and maximum overpressure are equivalent, for gases seeded with finite-size particles the maximum overpressure occurs downstream of the shock front (shown in Figure 8 and discussed below). In particular, we are interested in the pressure response away from the diaphragm in the decay region of the shock.

Although the Sommerfeld geometry is useful for comparison with experimental results, it is not the best geometry to use for gaining a complete understanding of characteristics of shock-particle interactions. There are several reasons for this. Although the driver section is long enough such that the expansion fan does not effect the shock front and shock wave Mach number (the quantity that Sommerfeld was most interested in), it does effect the area just behind the shock wave, making it more difficult to interpret temperature and pressure profiles obtained at different time intervals. This is especially apparent for the droplet vaporization

cases. In addition, the length of the driven section is such that only the transition region for the smallest particles and droplets can be captured. Finally, because we are also interested in the decay region of a shock wave produced from a shock tube, some simulations require a much smaller driver section and much longer driven section. Because of this, our results are split into two sections. One section describes results with a very large driver section. This is done to understand different aspects of shock waves impinging on seeded flow. The second set of results examines the decay region of the shock wave produced from a shock tube. All of the simulations for these results have a short driver section and long driven sections, and examine how the pressure decays as the shock wave propagates through the driven section. Because of our interest in mitigating the shock wave with either glass particles or water droplets, the seeded simulations are referred to as the *mitigated* cases, and the unseeded simulations as the *unmitigated* cases.

6 Propagation of Shock Waves through Seeded Gases

The geometry used for these simulations has a very large driver section (3 m), a small unseeded driven section (0.1 m), and a seeded section of 3-4 m. The small size for the unseeded driven section is adequate for the one-dimensional simulations to form the shock wave before it impinges on the seeded flow. Also, the small seeded region allows us to examine the effect of large particles or droplets penetrating into the high-temperature driver gas. The resolution used for these simulations was 1 mm per cell, which is good enough to give a smooth shock wave Mach number variation. Simulations computed with this geometry are indicated in Table 1. Only selected simulations are discussed in detail.

6.1 Representative case with glass particles

A representative solution (corresponding to case #1 in Table 1) is first examined with the long driver section mentioned above. The seeded regions contains a nearly mono-dispersed flow with one section and a diameter range from 26 μm to 28 μm. The mass-loading for all of these cases is $\eta = m^{(1)}/\rho = 0.63$. Snapshots of the solution for this specific case are shown in Figure 9 and Figure 10. Solution snapshots were taken at 1 ms intervals, to show the development of the shock wave as it interacts with the glass particles. Figure 9 shows the unmitigated shock wave results (solid lines) compared with the mitigated shock wave results (dashed lines). Figure 10 shows the gas-phase results (solid lines) compared with the dispersed-phase

Table 1: Simulations computed with the long driver section geometry. Length of driver section is 3 m, length of unseeded driven section is 0.1 m, and length of driven section is 3 m.

Case #	Dispersed-Phase	Mass Loading	Number Sections	Particle Size (μm)	Vaporization Model
1	None	0	NA	NA	
2	Glass	0.63	1	26-28	
2	Glass	0.63	1	13-14	
3	Glass	0.63	1	6.5-7	
4	Glass	0.63	NA	0	
5	Glass	0.63	1	4-6	
6	Glass	0.63	1	14-16	
7	Glass	0.63	1	24-26	
8	Glass	0.63	1	34-36	
9	Glass	0.63	1	49-51	
10	Glass	0.63	1	99-101	
11	Water	0.63	6	0-30	None
12	Water	0.63	6	0-30	Empirical-β
13	Water	0.63	6	0-30	Equilibrium
14	Water	0.63	6	0-60	Empirical-β
15	Water	0.63	6	0-15	Empirical-β
16	Water	0.63	6	0-120	Empirical-β
17	Water	0.63	12	0-30	Empirical-β
18	Water	1.26	6	0-51.3	Empirical-β
19	Water	0.315	6	0-17.54	Empirical-β
20	Water	0.63	6	0-60	Equilibrium
21	Water	0.63	6	0-15	Equilibrium
22	Water	0.63	6	0-120	Equilibrium
23	Water	0.63	12	0-30	Equilibrium
24	Water	1.26	6	0-51.3	Equilibrium
25	Water	0.315	6	0-17.54	Equilibrium

results (dashed lines) for the mitigated case.

The glass particles tend to have the maximum effect on the gas flow at the very front of the shock wave, where the velocity and temperature differences between the gas and the beads are largest. Behind the shock wave, the velocity and temperature of the beads (and gas) adjusts such that the momentum and energy exchange is lessened. Because of this effect, the solution snapshots appear rounded at the front of the shock wave, instead of having flat profiles as they do for the unmitigated cases (this is clearly shown in Figure 9.) Note that there still is a shock front with an associated pressure, density, and temperature jump, but the jump is much smaller than for the unmitigated case. It is also much lower than the maximum pressure developed behind the shock waves for the mitigated cases.

An interesting aspect of the mitigation studies is that the maximum pressure behind the shock wave is actually greater for the "mitigated" cases than for the non-mitigating cases (Figure 9c). The main reason for this seems to be an increase in gas density behind the shock wave for the mitigating cases (Figure 9a). This effect is predicted from the equivalent-gas analysis above, and is due to the compression wave generated by the gas slowing down. The left-moving reflected shock wave mentioned in the equivalent-gas analysis is seen in the 1 ms profiles at an axial location of around 0.4 m. It can be seen most easily in the velocity profiles in Figure 9f. Although a compressive shock, it is not sharp because momentum and energy equilibration is not instantaneous between the particles and gas.

The dispersed-phase solution is shown compared with the gas-phase solution in Figure 10. Here we see that the dispersed-phase eventually penetrates into the driver gas, as shown clearly in the density (Fig. 10a) and temperature (Fig. 10b) plots. The mass-loading of the dispersed-phase tends to spike to a maximum within the driver gas. This is caused by the larger viscosity within the driver gas (due to the higher temperatures) increasing the amount of drag felt by the glass particles. Whether the particles penetrate into the driver gas depends on the size of the unseeded section and the size of the particles, as we show later.

An $x - t$ diagram of the location of the shock wave (green), the contact discontinuity (red), and the particle interface (blue), as well as the shock wave Mach number is shown in Figure 11. The mitigated case is shown as a dashed line. Here we can clearly see that the glass particles penetrate past the contact discontinuity, and that both the contact discontinuity and the shock wave are slowed considerably by the

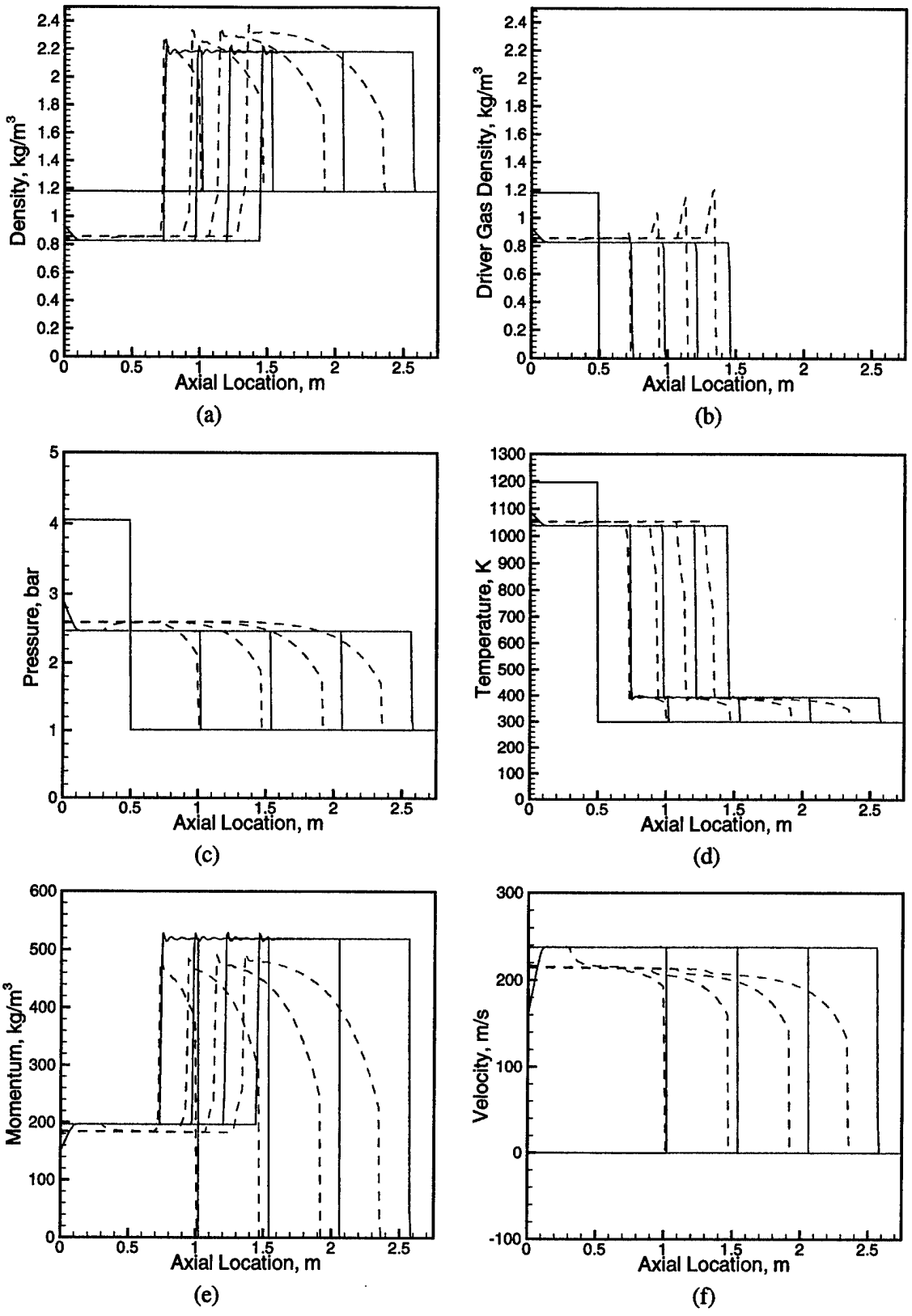

Figure 9: Snapshot of representative solution at 1 ms intervals for unmitigated (solid) and mitigated (dashed) shocks. $M_o = 1.49$, $\eta = 0.63$, 26-28 μm glass particles with large driver section geometry.

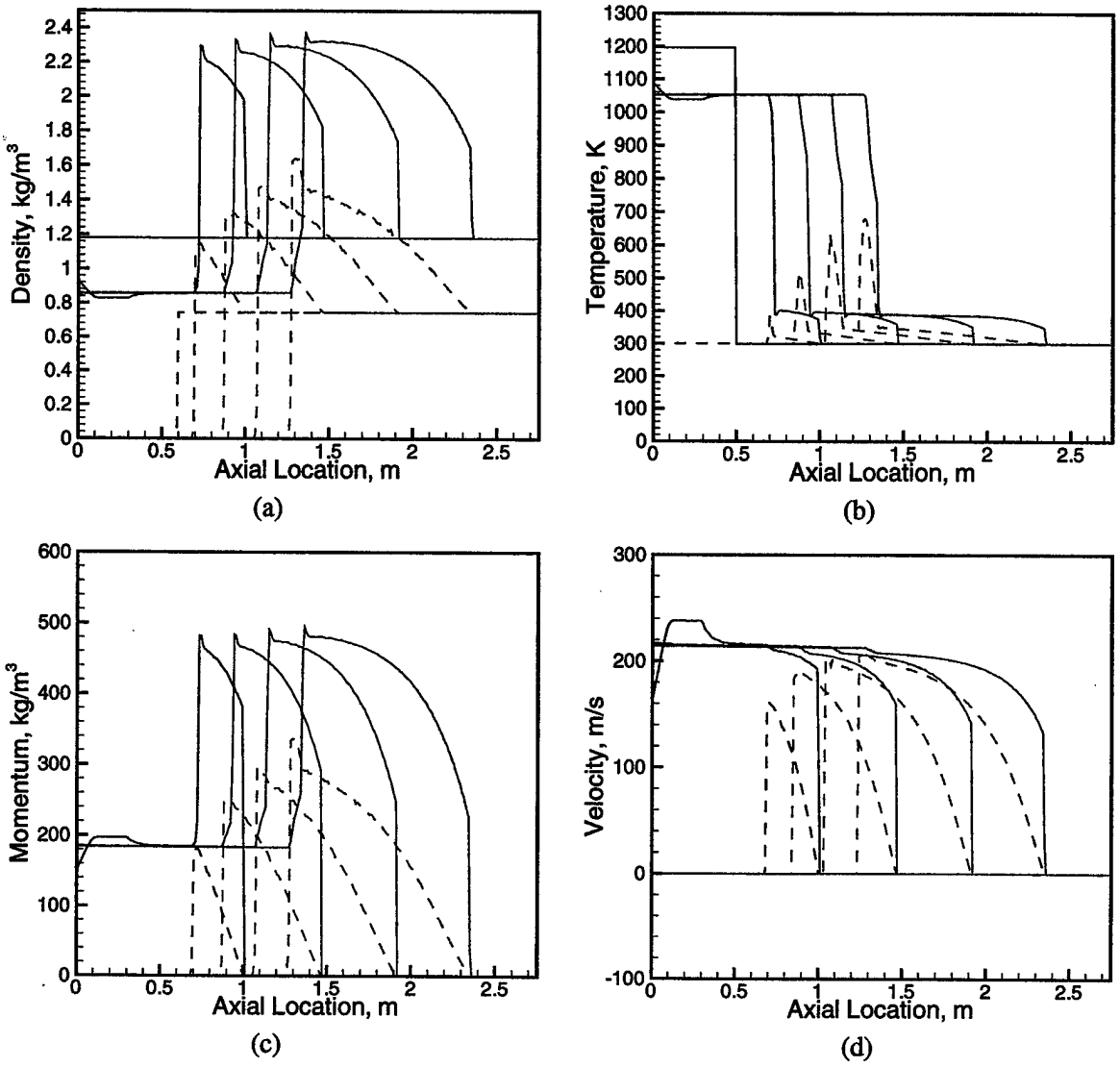

Figure 10: Snapshot of representative solution at 1 ms intervals for gas-phase (solid) and dispersed-phase (dashed) for the mitigating case. $M_o = 1.49$, $\eta = 0.63$, 26-28 μm glass particles with large driver section geometry.

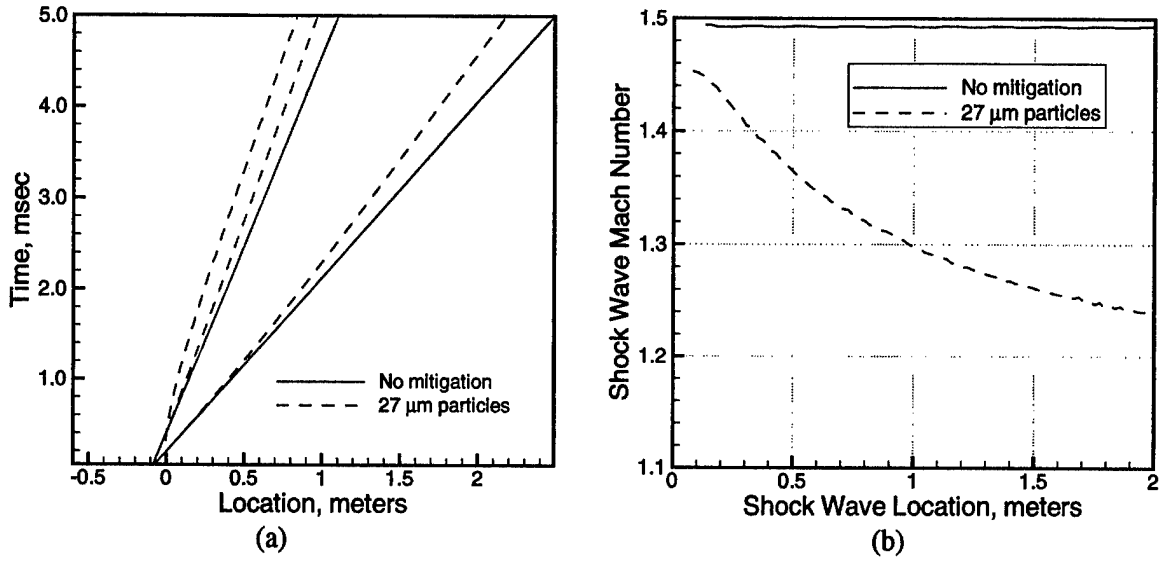

Figure 11: $x-t$ diagram (a) and shock wave Mach number (b) for representative mitigated and unmitigated cases. For the $x-t$ diagram, green indicates shock wave location, red indicates contact discontinuity location, and blue indicates particle interface. $M_o = 1.49$, $\eta = 0.63$, 26-28 μm particles with the extended driver section geometry.

particles. For the representative case, the shock wave Mach number does not reach the equilibrium value within the domain (Figure 11b).

6.2 Glass particle size effects

In addition to the above representative case, several other simulations were run with a similar geometry to determine the effect of particle size and mass-loading on the shock wave characteristics. Particle size has a significant impact on the mitigation produced by the glass particles. Changing the size of the glass particles changes the relaxation time required for the particles to reach equilibrium with the gas in terms of temperature and velocity. This affects how well the particles slow the initial shock wave down and penetrate into the driver gases. We examined droplet diameters ranging from 100 μm to infinitely small, with a mass-loading of $\eta = 0.63$. For the infinitely small particles, we assume the glass particles are in thermal and velocity equilibrium with the gas at all times.

Results from the simulations are shown in Figure 12 and 13. For infinitely small particles, the shock structure remains a square wave, although the shock wave itself is slowed down due to the additional mass being carried along with the shock. Although the shock pressure varies considerably with particle size, the

maximum pressure within the driven gases remains essentially the same and is independent of the particle size. Comparing the shock front pressure profile (Fig. 12a) at 1 ms, 2 ms, 3 ms, and 4 ms, the profile for the simulation with 27 μm particles changes as the shock wave moves downstream. The shock front pressure profile for the simulation with infinitely small particles does not change, and the profile for the simulation with very small particles (6.75 μm) only has small changes as the shock moves downstream. Again, this is related to the relaxation time associated with the different droplet size. At a certain point downstream, each profile reaches an equilibrium value after which the profile does not change (assuming the driver section is long enough that rarefaction waves do not effect the shock front) and the shock wave Mach number is constant.

Figure 13 shows the $x - t$ diagram and the shock wave Mach number as a function of location for similar cases. Note that both the 5 μm and the infinitely small particle cases shock Mach number have settled to the same equilibrium Mach number. Also note that the contact discontinuity has slowed down by almost exactly the same amount for all the mitigation cases regardless of the particle size. Note that the infinitely small particles very quickly reach the equilibrium value, whereas the finite size particles require considerable distance to reach this equilibrium value. This equilibrium value is only weakly dependent on the particle size, and is much more dependent on the mass-loading of particles.

Only the largest particles considered actually penetrated into the driver section for these cases. The amount that the particles penetrate into the driver gas is seen both in the $x - t$ diagram (Fig. 13a) and in the driver-gas density plot (Fig. 12b). Only for the 25 μm case have the particles penetrated into the driver gas.

6.3 Representative case with water droplets

Realistic mitigation systems would use water droplets and not solid particles, as in the simulations described previously. Our first results using water droplets for mitigation show snapshots of the solution with no vaporization, empirical-β vaporization (Eqn. 38), and with the equilibrium vaporization (Eqn. 39). The density profiles are plotted in Figure 14, and the temperature, pressure, and velocity profiles are plotted in Figure 15. As shown in Figure 14, the total density and the density of the air both rise sharply for the vaporization cases compared to the non-vaporizing case. This is because vaporization adds mass to the gas-phase and also compresses the gas-phase by slowing the shock wave down further. Looking at the

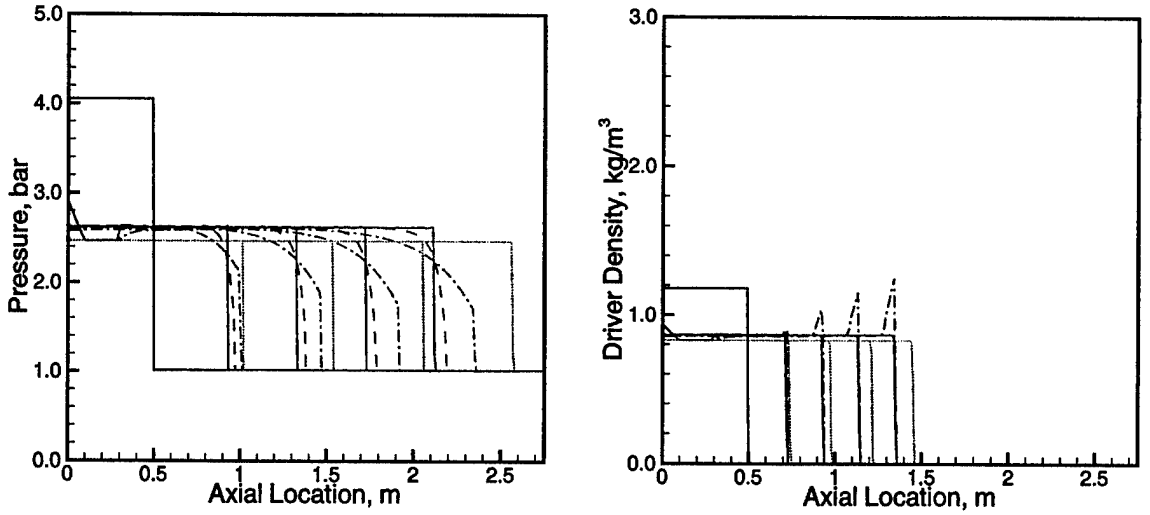

(a) (b)

Figure 12: Snapshot of pressure and driver density solutions at 1 ms intervals for shock waves mitigated with different size particles. Infinitely small (solid), 6.75 μm (dashed), 27 μm (dash-dot) particles are compared with the no mitigation solution (dotted). $M_o = 1.49$, $\eta = 0.63$, with the large driver section geometry.

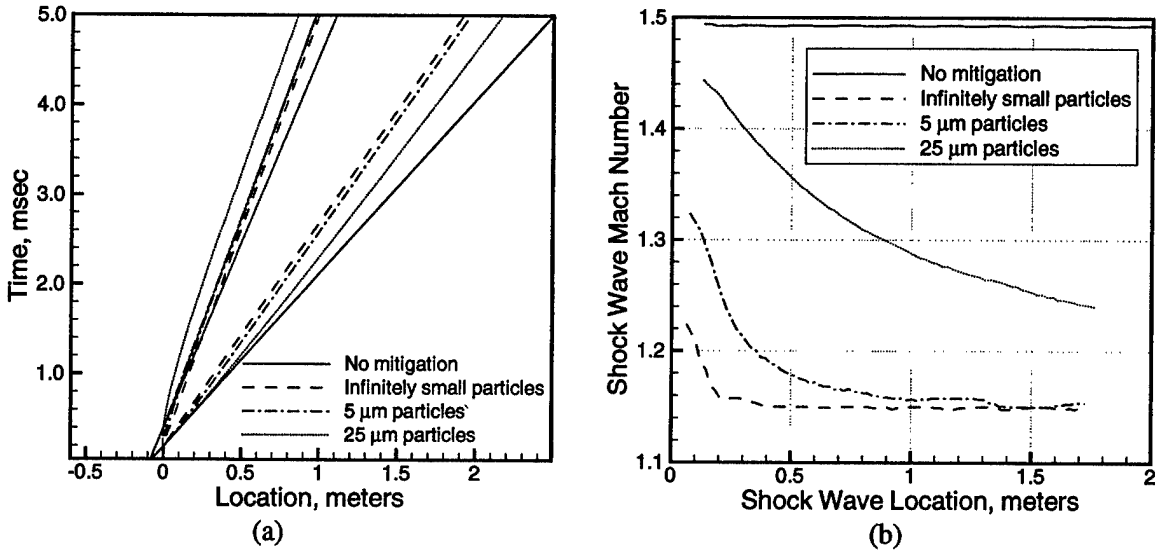

(a) (b)

Figure 13: $x - t$ diagram (a) and shock wave Mach number (b) for several different size glass particles. For the $x - t$ diagram, green indicates shock wave location, red indicates contact discontinuity location, and blue indicates particle interface. $M_o = 1.49$, $\eta = 0.63$, with the larger driver section geometry.

water vapor density, we see that the empirical-β vaporization model evaporates considerably more of the droplets than the equilibrium vaporization model, and most likely represents an upper bound on the amount of vaporization taking place.

Some interesting aspects of Figure 15 should be pointed out. For both vaporization cases, the temperature is reduced significantly. For the empirical-β vaporization, the temperature in the shocked driven gases goes down to the cut-off temperature of 310 K, at which point no further vaporization takes place and the temperature remains constant. Although the temperature and density have both changed significantly with vaporization, the effects of these changes tend to cancel out such that the resulting shock pressure remains approximately the same (it is actually slightly lower for high levels of vaporization).

Another interesting result is the total water mass in each of the sections. This quantity tells us how much water has evaporated, and how much mass has transferred between the different sections. The integrated mass is shown in Figure 16. Because of the large differences in mass between sections, the y-axis is shown as a log plot, although within each section the relationship between integrated mass and time is more linear than exponential. The interesting aspect of this plot is how little mass has actually evaporated. Finally, the effect of vaporization on the shock wave Mach number is shown in Figure 17.

The small amount of vaporization seen in Fig. 16 is due primarily to the low temperature of the shocked driven gases (about 400 K). The vaporization reduces this temperature quite rapidly to the limiting temperature for vaporization (for this study, the limiting temperature is set to 310K). This is a limitation of the present simulations, and only studies with stronger shocks will show the effect of appreciable vaporization.

Also of interest is the considerably lower amount of vaporization for the equilibrium model as opposed to the empirical-β model. There are several reasons for this result, some of which are physical and others are limitations of the model. First, the amount of vaporization for the equilibrium model is closely coupled to the temperature of the droplet. At low temperatures, the amount of vaporization is minimal, and much of the heat flux to a droplet is used to increase the temperature of the droplet. Only after the droplet is heated will the vaporization rate become large. This is physically realistic and is an important improvement over the empirical-β model. However, because we are using the infinite conductivity model, we once again artificially limit the surface temperature of the droplet by requiring the entire droplet to be at a constant

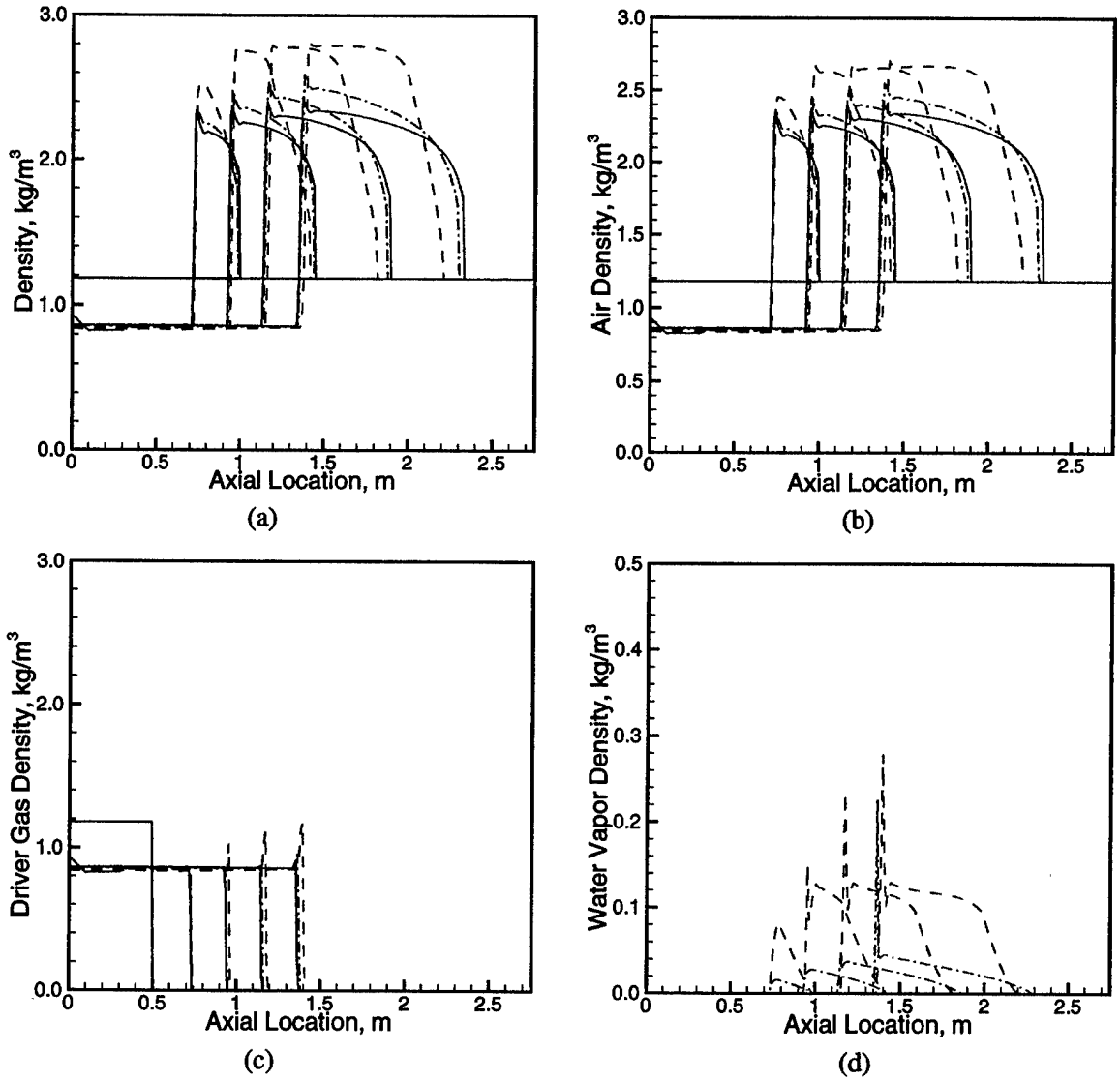

Figure 14: Snapshot of density solutions for the representative water droplet case at 1 ms intervals for gas-phase. $M_o = 1.49$, $\eta = 0.63$. Water droplets initially evenly dispersed from 25 μm to 30 μm. No (solid), temperature-dependent (dashed), and equilibrium (dash-dot) vaporization.

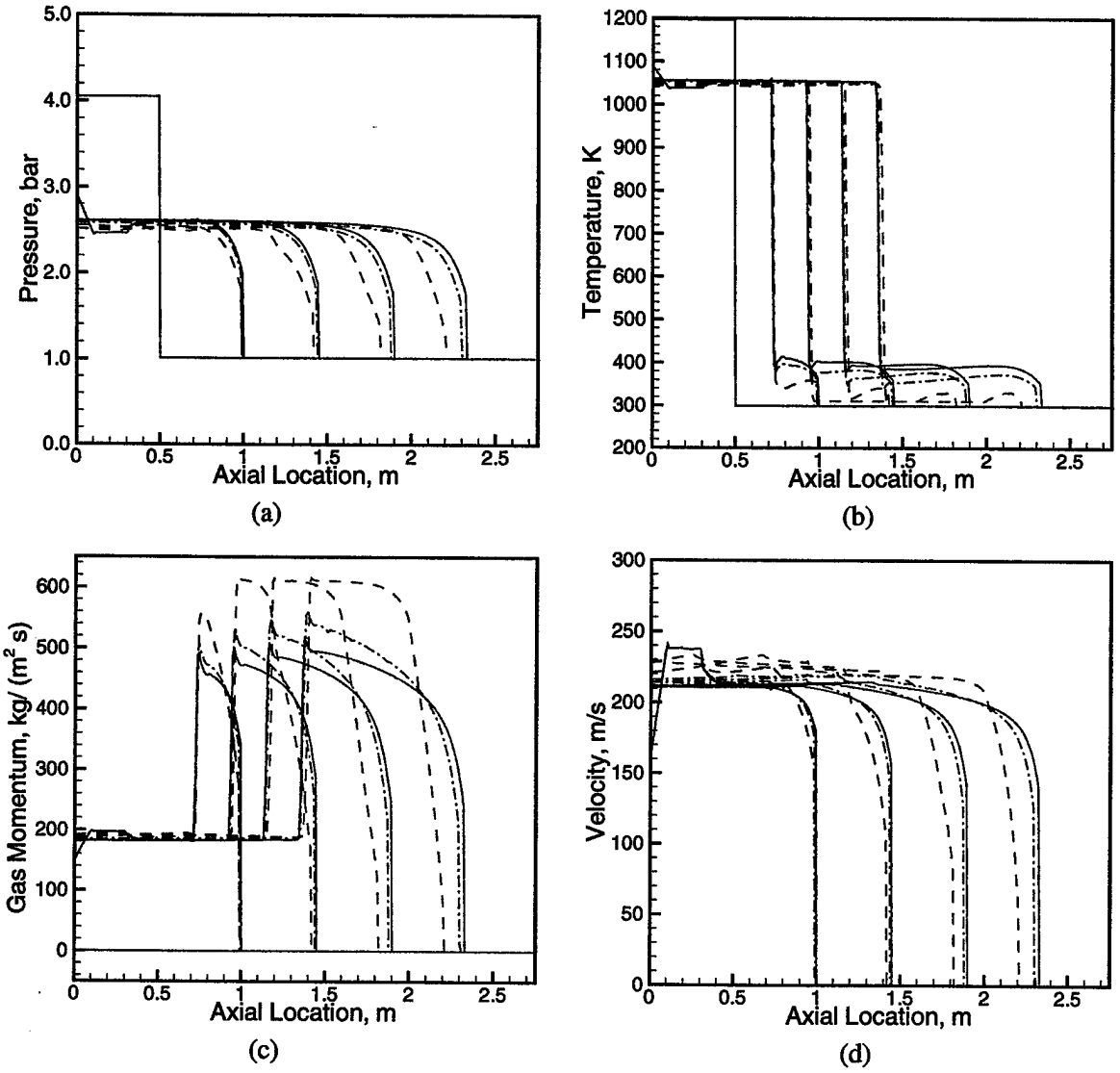

Figure 15: Snapshot of solutions for the representative water droplet case at 1 ms intervals for gas-phase. $M_o = 1.49$, $\eta = 0.63$. Water droplets initially evenly dispersed from 25 μm to 30 μm. No (solid), temperature-dependent (dashed), and equilibrium (dash-dot) vaporization.

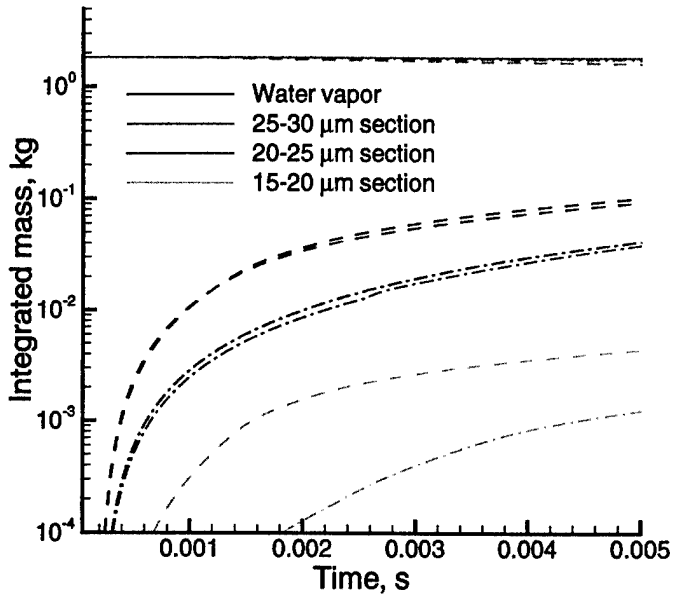

Figure 16: Total integrated mass of water in individual sections for the representative water droplet cases. $M_o = 1.49$, $\eta = 0.63$. Water droplets initially evenly dispersed from 25 μm to 30 μm.

temperature. Near the shock front (where vaporization will be most important), however, the outer region of the droplet will be at a higher temperature and allow for more vaporization than the interior regions of the droplet, and thus the vaporization rate will be higher than that predicted by the infinite conductivity model. Also, because of the extremely high velocities encountered within the shock, the correlations currently used for convective effects may be inadequate. Therefore we feel that the equilibrium model represents a lower bound on vaporization, while the empirical-β model serves as a useful upper bound.

6.4 Water droplet size effects

Two parametric studies were done to examine the effect of droplet size on shock mitigation. The first study keeps the mass-loading of water droplets constant, while varying the droplet size. This has the effect of also changing the number density of the droplets. The second set of cases keeps the number density constant while varying the droplet size. The results (in terms of shock wave Mach number) are shown in Figure 18. As can be seen comparing the two figures, the equilibrium value for the shock wave Mach number appears to be closely tied to the mass-loading and relatively independent of droplet size (apparent when comparing the 12.5-15 μm and the 25-30 μm results), even though close to the diaphragm the mitigation curves for the

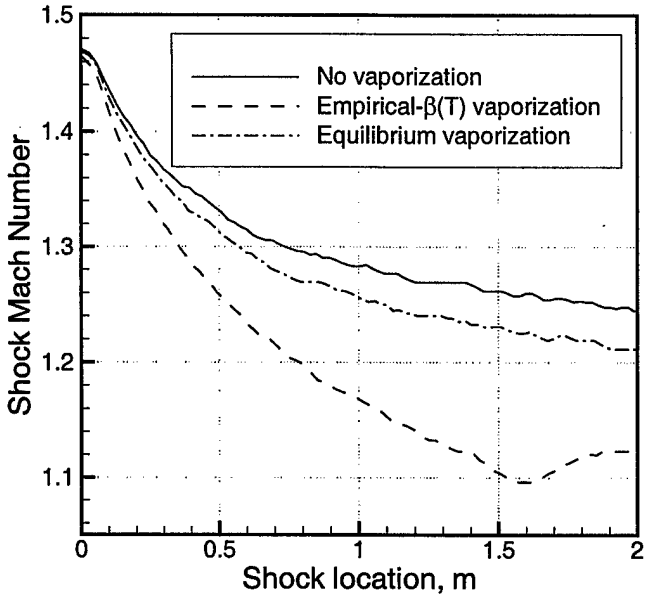

Figure 17: Effect of vaporization on shock wave Mach number for the representative water droplet cases. $M_o = 1.49$, $\eta = 0.63$. Water droplets initially evenly dispersed from 25 μm to 30 μm.

constant number-density cases appear to more closely resemble each other. This may imply that the initial region may be more dependent on vaporization processes, whereas the equilibrium region is more dependent on the mass-loading, however, the results are not conclusive in this respect.

7 Shock Wave Decay in Seeded Gases

One of the key observations made in the section above is that maximum overpressure is greater for the "mitigated" cases than the unmitigated cases. Therefore, one may think that injecting glass particles into the flow is rather poor at mitigating the effects of the blast overpressure. However, we now examine some cases with much smaller driver sections. These cases have a much shorter driver section of 0.5 m, while the seeded driven section and the unseeded driven section remain the same at 3.4 m and 0.1 m respectively. In these cases, the reflected rarefaction waves play an important role in the shock wave dynamics.

7.1 Representative case with glass particles

A representative solution was first run with identical gas and particle conditions as the representative solution with the long driver section. The seeded region contains a nearly mono-dispersed flow with one

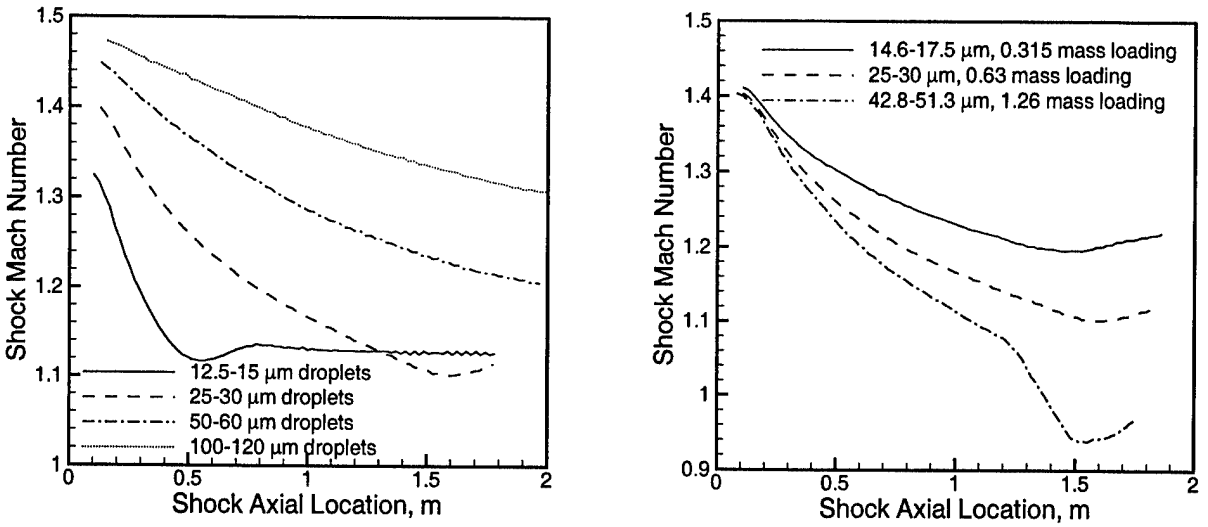

Figure 18: Effect of droplet size on shock wave Mach number. Mass-loading of water droplets is held constant at 0.63 (a), number-density is held constant (b). $M_o = 1.49$. Empirical-β vaporization model is used.

Table 2: Simulations computed with the short driver section geometry. Length of driver section is 0.5 m for all simulations.

Case #	Dispersed-Phase	Section Length Unseeded	Section Length Seeded	Mass Loading	Number Sections	Particle Size (μm)	Vaporization Model
1	None	0.1	3	0	NA	NA	
2	Glass	0.1	3	0.63	1	26-28	
3	None	0.5	10	0	NA	NA	
4	Glass	0.5	10	0.63	NA	0	
5	Glass	0.5	10	0.63	1	4-6	
6	Glass	0.5	10	0.63	1	9-11	
7	Glass	0.5	10	0.63	1	19-21	
8	Glass	0.5	10	0.63	1	39-41	
9	Glass	0.5	10	0.63	1	59-61	
10	Glass	0.5	10	0.63	1	99-101	
11	Water	0.1	3	0.63	6	0-30	None
12	Water	0.1	3	0.63	6	0-30	Empirical-β
13	Water	0.1	3	0.63	6	0-30	Equilibrium
14	Water	0.1	3	0.63	6	0-60	Empirical-β
15	Water	0.1	3	0.63	6	0-15	Empirical-β
16	Water	0.1	3	0.63	6	0-120	Empirical-β
17	Water	0.1	3	0.63	12	0-30	Empirical-β
18	Water	0.1	3	1.26	6	0-51.3	Empirical-β
19	Water	0.1	3	0.315	6	0-17.54	Empirical-β

section and a diameter range from 26 μm to 28 μm. The mass-loading for all of these cases is $\eta = m^{(1)}/\rho = 0.63$. As before, we show the gas-phase solution profiles at 1 ms intervals for the mitigated and unmitigated cases in Figure 19. For the unmitigated simulations, we see the classical shock-tube behavior. Even before 1 ms, the rarefaction wave has reflected off the back wall. The rarefaction wave then tends to reduce the pressure just behind the shock wave until it finally reaches the shock front and affects the shock wave. The rarefaction wave also lowers the temperature behind the shock wave and substantially slows down the driver gases.

Comparing the unmitigated (dashed) and the mitigated (solid) pressure results in Figure 19c, the overall pressure is clearly reduced for the mitigation simulations away from the initial diaphragm (after approximately $x = 1.2$ m). Because of the shape of the pressure profiles for the mitigated studies, the rarefaction wave has less far to travel to relieve the maximum overpressure for the shock front, and thus reduces the maximum overpressure much more quickly than the unmitigated case. The same is true for the momentum, density, and velocity within the shock front.

Figure 20 shows the gas-phase and particle-phase profiles for the representative solution. The particle-phase profiles tend to follow the same behavior as for the mitigation cases with long driver sections. One difference is found in the temperature solutions, Figure 20b. For the long driver sections, the particles reach a high-temperature only within the driver gases. For the mitigated cases, the particle temperature increases past the contact discontinuity, but then this high temperature moves into the region of flow with the driven gas. The reason for this is that the driver gas is being slowed by the rarefaction wave. Because the particles adjust to the gas velocity slowly (as shown in Figure 20d), the particles move from the driver gas back into the driven gas. This is also why we see a higher velocity for the mitigated cases away from the initial shock, such as in Figure 19f for the 4 ms (red) results.

Close to the diaphragm, before the rarefaction wave affects the shock front (at a time of 1 ms), the pressure for the mitigated cases is slightly greater than the unmitigated cases. Further downstream, however, shown in Figure 19c, the overpressure does decrease for the mitigation cases. To quantify better the resulting overpressure decrease due to the glass particles for specific distances from the diaphragm, pressure sensors were placed at 5 cm intervals in the seeded driven section of the shock tube. Taking the maximum

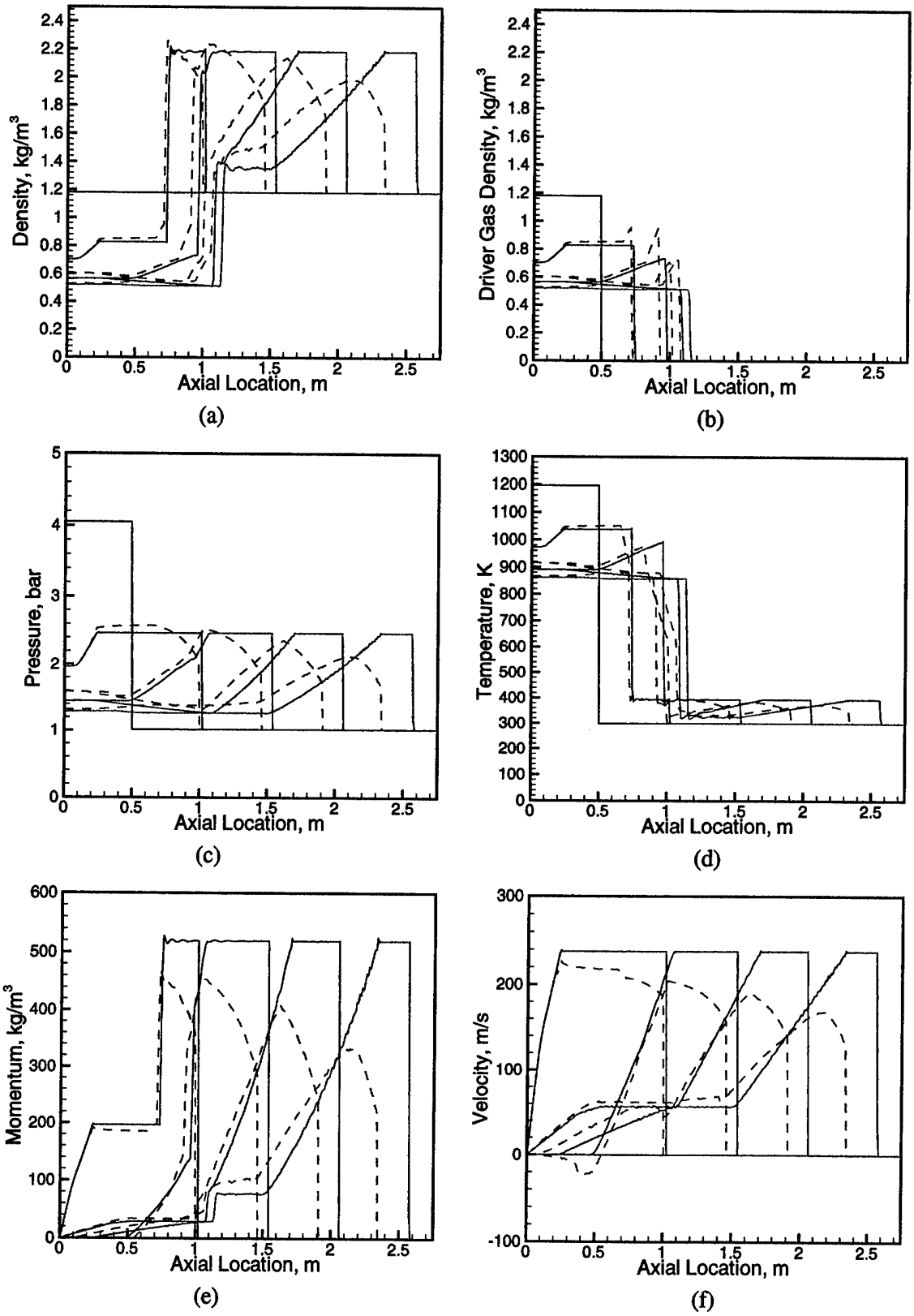

Figure 19: Snapshot of representative solution at 1 ms intervals for unmitigated (solid) and mitigated (dashed) shocks. $M_o = 1.49$, $\eta = 0.63$, 26-28 μm particles with small driver section geometry.

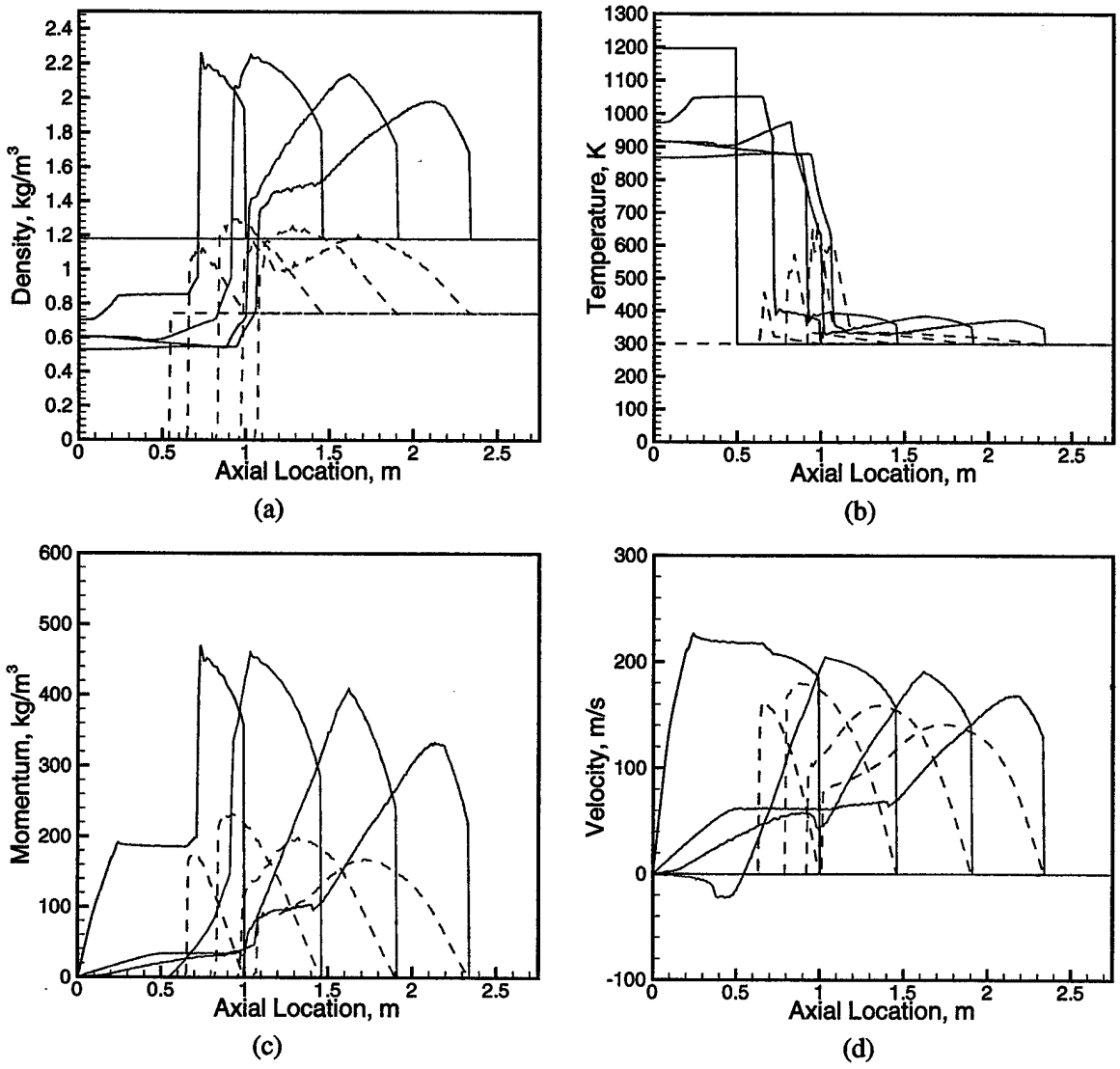

Figure 20: Snapshot of representative solution at 1 ms intervals for gas-phase (solid) and dispersed-phase (dashed) for the mitigating case. $M_o = 1.49$, $\eta = 0.63$, 26-28 μm particles with small driver section geometry.

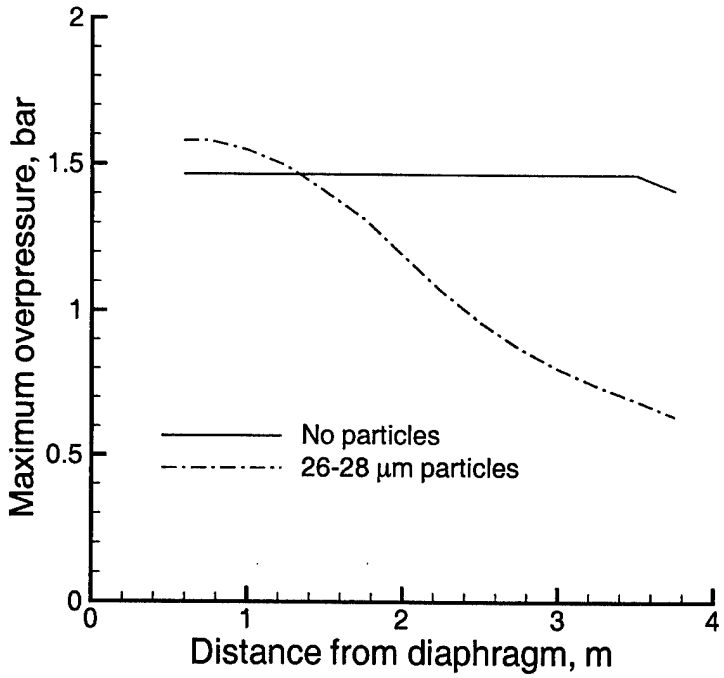

Figure 21: Maximum overpressure for representative solution as a function of sensor location. $M_o = 1.49$, $\eta = 0.63$, 26-28 μm particles with small driver section geometry.

overpressure at each point and plotting it versus sensor location, the amount of pressure mitigation observed for a given distance from the initial diaphragm is quantified. This is plotted in Figure 21 to give a good idea of the amount of mitigation to be expected for the given geometry.

7.2 Glass particle size effects

Important to this study is a determination of the effect of particle size on the mitigation characteristics of shock waves in seeded gases. A parametric study of particle size was done using the same set up as described above for the representative solution. The size of the driven section is extended to 10 meters such that we capture a larger portion of the decay region of the shock wave. The diaphragm is located at axial location $x = -0.5$ m such that the unseeded/seeded interface is now at the origin.

The range of sizes considered for the parametric study varied from infinitely small particles (equivalent-gas formulation) to 100 μm particles. The results are divided into two groups: small particles (particles smaller than around 40 μm) and large particles (particles larger than around 40 μm). The pressure profile at five ms intervals is shown in Figure 22 for several different particle sizes. Fig. 22a shows the smaller particle group, and Fig. 22b shows the larger particle group. With the smaller driver section, attenuation starts very

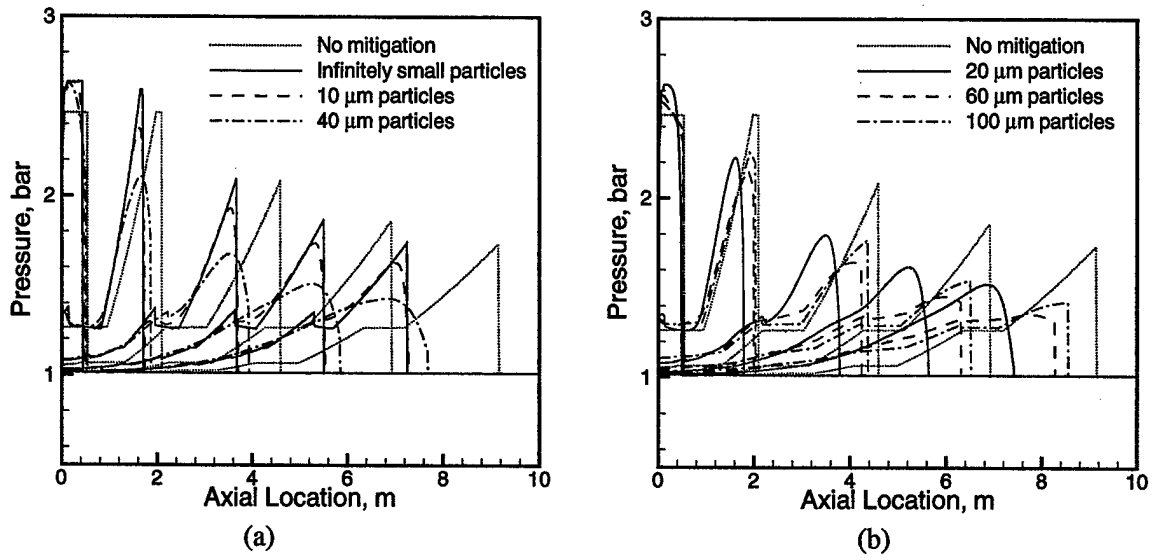

Figure 22: Snapshots of pressure profiles at 5 ms intervals for particle size study. $M_o = 1.49$, $\eta = 0.63$, with the small driver section geometry (0.5m) and an extended seeded driven section (10m).

soon after the diaphragm breaks. The dotted line for both plots indicate an unmitigated case. Attenuation of the unmitigated shock wave begins about 2 m downstream from the seeded/unseeded interface (about 2.5 m from the diaphragm). Attenuation of the mitigated shocks begins before that, as we saw in the representative case. Looking at the smaller particles, as the size increases, the peak pressure that is sharp for the infinitely small particles becomes rounded and more diffuse for the larger particles. This is especially apparent for the largest particles shown in Fig. 22a, which shows considerably more overpressure reduction than the smaller particle cases, but less reduction in the shock wave velocity .

For the larger droplets, a different trend is evident. Early in the calculation (at 0.01 seconds) the pressure profiles for the largest particles (60 μm and 100 μm) still resembles the unmitigated pressure wave (although the maximum pressure is reduced substantially). At this point, the flow is still transitioning from the unmitigated profile to the mitigated equilibrium profiles. During this transition, the pressure is not reduced as fast as the smaller particle cases. However, once the transition is complete, the pressure reduction becomes much greater, and is more similar to the smaller particle cases.

The above 2 sets of results suggest that there is an optimum droplet size. Another way of look at the results is given in Figure 23. These plots show the maximum overpressure felt at any point downstream of the seeded/unseeded section interface. Again, the plot is divided into two groups dependent on the particle

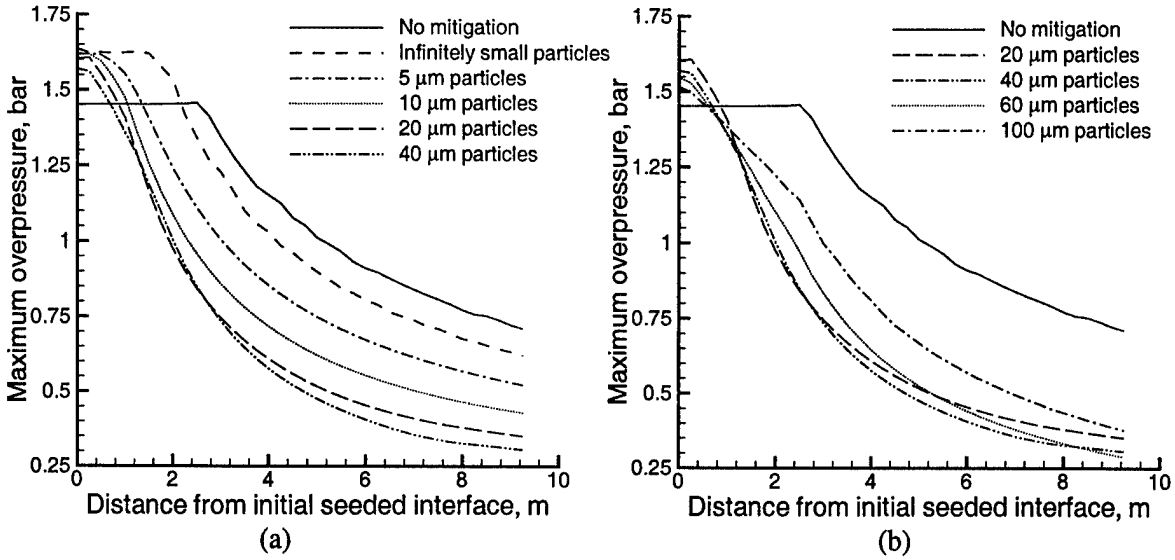

Figure 23: Maximum overpressure as a function of sensor location. $M_o = 1.49$, $\eta = 0.63$, with the small driver section geometry (0.5m) and an extended seeded driven section (10m).

size for clarity of presentation. The graph of smaller droplets (Figure 23a), shows that increasing the size clearly increases the amount of pressure reduction up to about 40 μm. At this point, the plot becomes much more difficult to interpret because during the initial phases of decay, the shock wave is still transitioning to its equilibrium setup with respect to the particles. Thus the deceleration of the shock wave is slower, until it completes the transition at which point it increases. This effect is more clearly shown for the larger particles in Fig. 23b.

7.3 Representative case with water droplets

As before, we first examine the effect of the vaporization models on the decay characteristics of the shock wave for a representative case. This representative solution uses the same conditions as the previous representative solution for glass particles, except that water droplets are used instead of glass particles. The density, pressure, and temperature profiles are shown in Figure 24. As with the glass particles, downstream from the diaphragm the pressure is reduced for mitigated cases compared with the unmitigated case, with the greatest reductions in maximum overpressure seen with vaporization. Also interesting to note is that the temperature goes below 300 K for both vaporization cases. This is because the droplet vaporization tends to reduce the temperature drastically before the rarefaction wave reflects and penetrates into the driven

gases, as demonstrated in Figure 15b for steady shock waves. When the rarefaction wave penetrates into the driven gases, the temperature is further reduced, at which point it goes below 300 K. Currently there is no condensation model in the program, but clearly some condensation may occur at this point raising the temperature. The total integrated mass in several sections is shown in Figure 25.

In terms of mitigation, we again have pressure sensors spaced 25 cm apart. Plotting the maximum overpressure for each sensor in Figure 26 and comparing the non-mitigating and mitigating cases, we clearly see the effect of vaporization on the maximum overpressure felt at any location. Interesting to note is that the equilibrium vaporization model initially gives results similar to the non-evaporating results; however, by the end of the domain the maximum overpressure is close to the empirical-β vaporization results. This is because the equilibrium model produces much smaller vaporization rates initially, until the surface of the droplets increase in temperature; however, as the shock wave continues to travel the total amount of vaporization tends to approach the amount vaporized with the empirical-β model (Figure 25.)

7.4 Water droplet size effects

The next set of simulations looked at the effect of droplet size on mitigation of the maximum overpressure. As with the previous studies on droplet size, we do two sets of simulations and compared the results. All of these cases used the empirical-β vaporization model. The first set kept the mass-loading constant at 0.63 and varied the droplet size from 12.5-15 μm to 100-120 μm. The second set of computations kept the number density constant for all cases and varied the mass-loading with the particle size.

The results for maximum overpressure as a function of location for both series of computations are shown in Figure 27. Because the shock wave is fairly weak, the temperature of the shocked driven gases only reaches about 400K, and this is rapidly cooled by evaporation of only a small part of the water available. Because of this, the parametric study with the mass-loading constant (Fig. 27a) follows closely the characteristics of the glass particle study presented earlier in this report.

The parametric study keeping the number density constant as the droplet size and mass-loading varies is shown in Fig. 27b. The idea behind this study is that for the smaller droplets, a larger percentage of the available water is able to vaporize, thus the reduction in pressure (relative to the larger droplets and larger mass-loading) is more similar even though much less water is used. From the results, it is difficult to tell

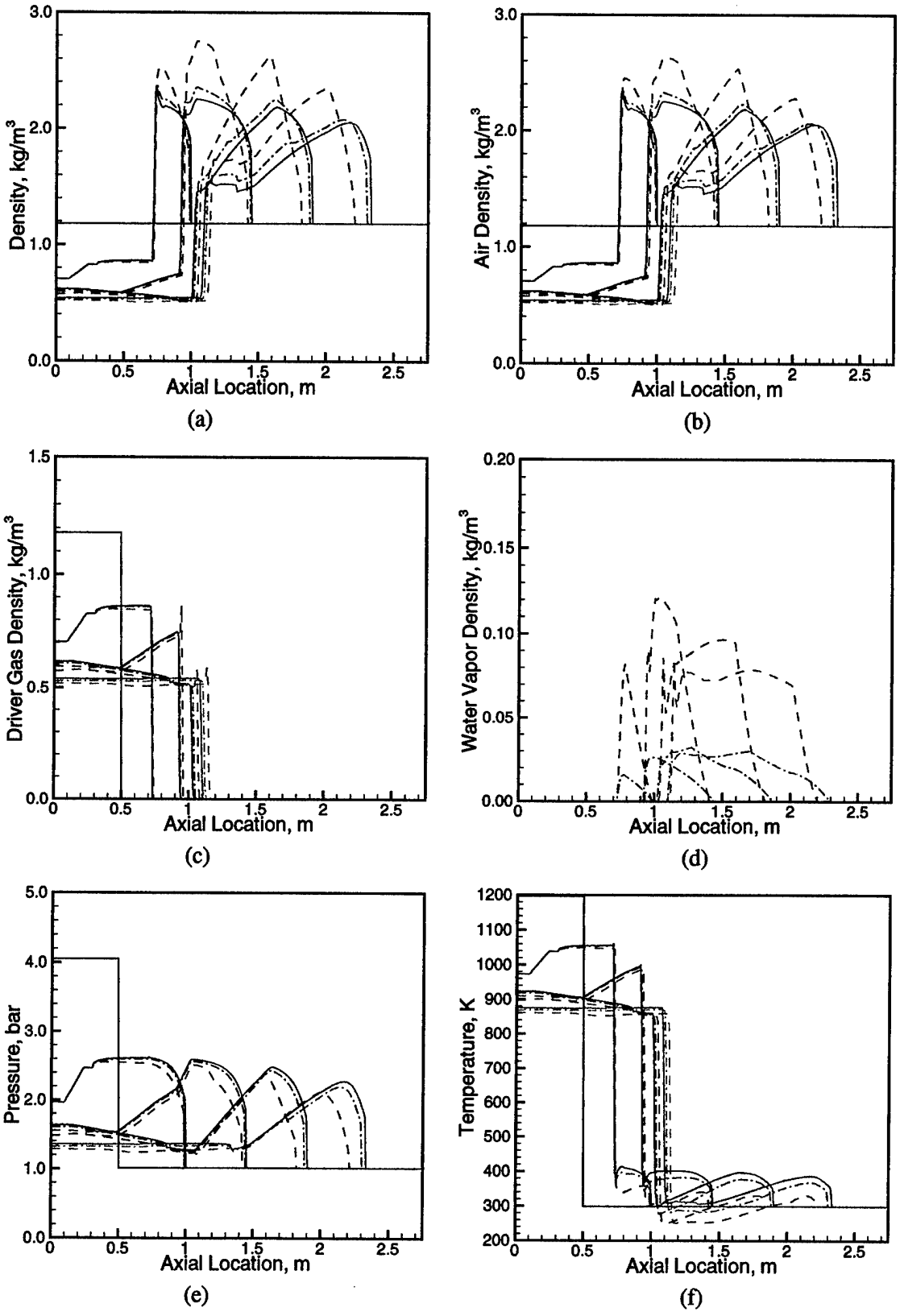

Figure 24: Snapshot of solution for representative water droplet case at 1 ms time intervals. $M_o = 1.49$, $\eta = 0.63$, with short driver section geometry. Water droplets initially evenly dispersed from 25 μm to 30 μm. No (solid), temperature-dependent (dashed), and equilibrium (dash-dot) vaporization.

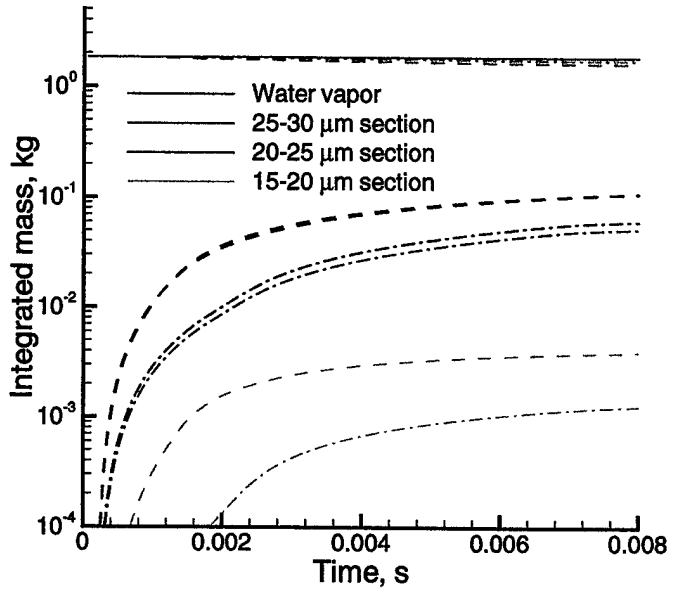

Figure 25: Total integrated mass of water in individual sections for representative water droplet case. $M_o = 1.49$, $\eta = 0.63$, with short driver section geometry. Water droplets initially evenly dispersed from 25 μm to 30 μm. No (solid), temperature-dependent (dashed), and equilibrium (dash-dot) vaporization.

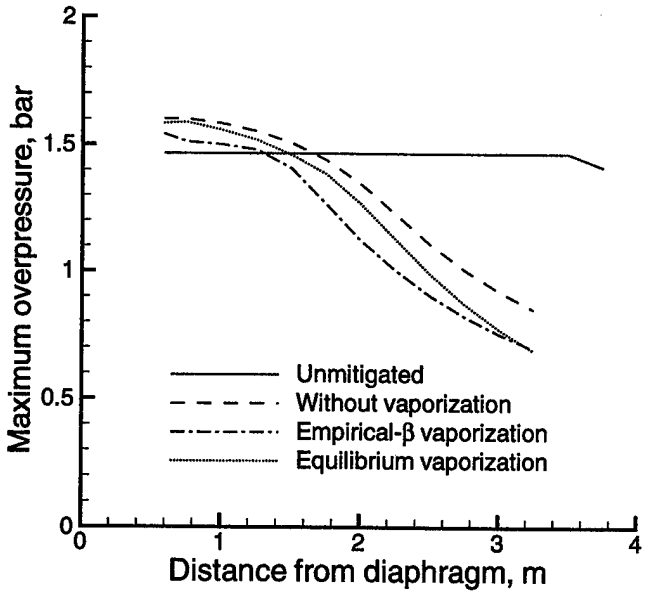

Figure 26: Maximum overpressure as a function of sensor location. $M_o = 1.49$, $\eta = 0.63$, with the small driver section geometry.

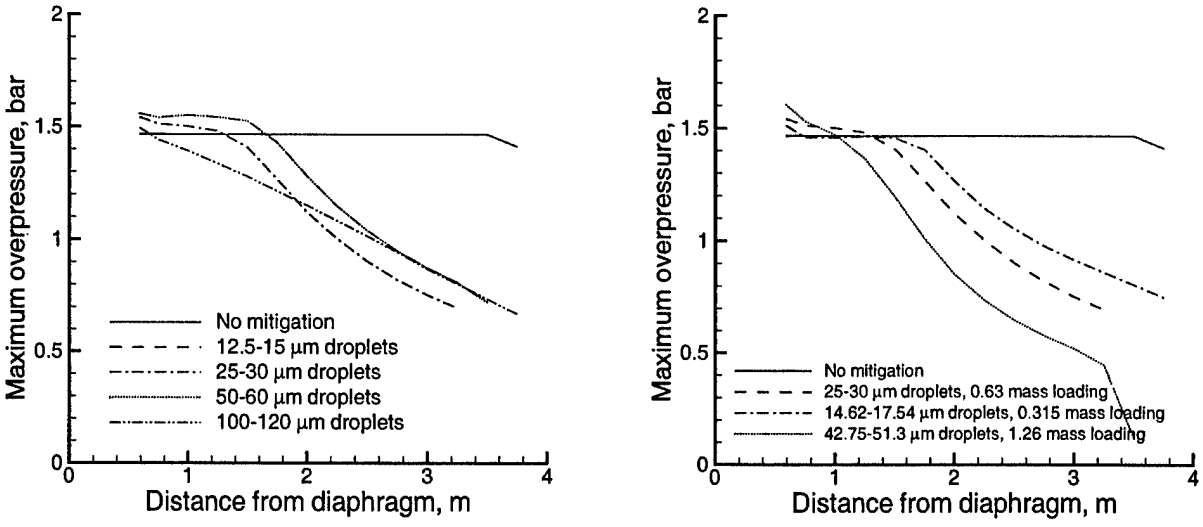

Figure 27: Maximum overpressure for different droplet sizes with mass-loading held constant at $\eta = 0.63$ (left), and with number density held constant (right). $M_o = 1.49$, with the small driver section geometry.

whether there is any benefit from using smaller droplets and a smaller mass-loading. Part of the reason for this is that it is not appropriate to keep the number density constant. A more appropriate study would keep the surface area constant between different droplet sizes, thus the amount of vaporization is similar. For our case, there will still be more total vaporization for the larger droplet cases, even though the percentage of water evaporated is smaller. Apart from this, these cases suffer from the same problem as the other vaporization studies; namely, that the shock wave is too weak to create high temperatures in the shocked gases, limiting the amount of vaporization that will occur.

8 Summary and Conclusions

Because of the number of simulations conducted for this report, we first summarize our results before presenting conclusions discussing the relevance to blast mitigation. The report started with a summary of shock relations for transmission of shock waves through particle-laden flows for infinitely small particles. From this analysis, it was found that for most cases, transmission of the shock wave results in compression of the particle-laden gases by a reflected shock wave. an increase in the overpressure behind the shock wave and a decrease in the shock wave velocity. The increase in overpressure is caused by compression of

the gases due to lower gas velocities. This analysis, however, did not account for particle size effects or vaporization effects, which requires a numerical treatment.

The sectional approach for dispersed-phase numerical simulations was consequently developed for a convective flow-field. This approach allows the dispersed-phase to be treated by continuum conservation equations. Cross-coupling terms between the gas and dispersed-phase, and between the different sections in the dispersed-phase were developed using single-droplet models. The infinite conductivity model was used for calculating the energy of the particles, and the equilibrium vaporization model was used for calculating vaporization rates with corrections to account for convective effects. The sectional approach was then incorporated into a high-speed computational fluid dynamics code based on the flux-corrected-transport algorithm.

The numerical methodology was first validated using experimental data. The experiments investigated the transition of the shock wave from unseeded gases to gases seeded with glass particles. Good agreement was found with the results for different Mach number shock waves and different mass-loading of particles. Interestingly, it was found that better agreement could be found at the beginning of the transition region for simulations that did not include heat transfer, although these simulations generally did not get the equilibrium shock wave Mach number correct. This is most likely caused by the infinite conductivity model, which keeps the particle surface temperature artificially low initially, thus overpredicting heat transfer to the particles.

Further simulations were conducted to examine the mitigation characteristics of steady and decaying shock waves impinging on seeded flows. First, we simulated the effects of steady shock waves, produced using shock tubes with long driver sections. We described both the effect of non-vaporizing particles and vaporizing droplets on the pressure and velocity of the shock wave. We found that although seeding the flow generally causes the shock wave to slow down, the pressure developed behind the shock wave actually increases in particle-laden flows. For infinitely small particles, the square wave form is maintained, however, for finite sized particles the shock structure is spread out such that the maximum overpressure is developed downstream of the actual shock front. With vaporization, the temperature is reduced considerably. The pressure, however, is reduced only slightly because the density of the gas has now also increased significantly

due to the water vapor. For the cases presented in this report, the amount of vaporization is quite small due to the weak shocks we investigated, which result in only moderate temperatures for the shocked driven gases.

Another set of simulations examined decaying shock waves, produced using shock tubes with short driver sections. Again, we looked at the effect of different particle sizes on the velocity of the shock wave and the pressure developed behind the shock front. Unlike the steady shock waves, the maximum overpressure for decaying shock waves is reduced for the particle-seeded simulations. This effect is caused because the droplets tend to disperse energy away from the sharp peak. As the particle size increases, this effect becomes more pronounced. However, there is a conflicting effect. If the shock wave has not fully transitioned to the final shock structure corresponding to the equilibrium condition, the particles are not as effective in dispersing the energy away from the sharp peak. This results in higher maximum overpressures compared to smaller droplets. The effect of vaporization for these cases is to further reduce the maximum overpressure felt at specific locations. The degree to which the maximum overpressure is reduced depends on the amount of vaporization that occurs. For the simulations done, we found a small overall reduction in maximum overpressure and a somewhat larger reduction in the velocity of the shock wave. As for the previous studies, the small effect of vaporization on the maximum overpressures is due to the low temperature of the shocked driven gases.

Additional studies are required to further quantify the effects of water droplets on blast mitigation and how to effectively mitigate them. In particular, vaporization needs to be more closely studied. These simulations indicated that vaporization decreases the air temperature significantly, but only has a small effect on the shock overpressure. Because of the low temperatures in the shocked driven gases for these cases, vaporization had only a secondary role in the mitigation studies conducted above. A stronger shock wave is essential to allow the vaporization to have a more critical role in mitigating the shock wave produced from either a blast or a shock tube.

Blasts from explosives are in many ways similar to the shock tube flows used for this study. The initial explosive is analogous to the shock tube driver section, and acts to form the shock wave after the energy is released. For blasts, because of the small size of the explosive and the fact that most blasts spherically emanate from the initial explosive (unlike shock tubes, which are usually planar), the shock wave for the

blast almost instantly starts decaying. From the simulations with the planar shock wave, we would expect a particle-laden flow to effectively mitigate this type of shock wave since it is similar to the decaying shock waves discussed in this report.

Although shock tubes and explosive blasts share many similarities, they also have significant differences. In addition to the previously mentioned difference between planar and spherical shock wave, explosive blasts have density ratios that are significantly greater (by orders of magnitude) than these produced in a shock tube. Also, many explosives are oxygen-deficient, and thus have reactions occurring within the driver gases. Penetration of the droplets into the driver gas region will lead to additional mitigating effects. Although numerical simulations may guide experimental work for determining mitigation of explosive blasts from water mist, experimental work is crucial in determining the validity of the simulation technique and for refining the models to the extreme environments found for explosive blasts.

Acknowledgements

This work is sponsored by the Office of Naval Research through Code 334 Damage Control Task and the NRL 6.1 Computational Physics Task Area.

References

[1] K. Kailasanath, P.A. Tatem, F.W. Williams, and J. Mawhinney. "Blast Mitigation Using Water—A Status Report." Technical Report NRL/MR/6410–02-8606, Naval Research Lab, 2002.

[2] D.A. Schwer and K. Kailasanath. "Blast Mitigation by Water Mist (1) Simulation of Confined Blast Waves. Technical Report NRL/MR/6410–02-8636, Naval Research Lab, 2002.

[3] W.A. Keenan and P.C. Wager. "Mitigation of Confined Explosion Effects by Placing Water in Proximity of Explosives." In *25th DoD Explosives Safety Seminar*, Anaheim, CA, August 18-20 1992.

[4] W. A. Sirignano. *Fluid Dynamics and Transport of Droplets and Sprays.* Cambridge University Press, Cambridge, UK, 1999.

[5] D.D. Joseph, J. Belanger, and G.S. Beavers. "Breakup of a liquid drop suddenly exposed to a high-speed airstream." *Intl. J. Multiphase Flow*, 25:1263–1303, 1999.

[6] D.D. Joseph, G.S. Beavers, and T. Funada. "Rayleigh-Taylor instability of viscoelastic drops at high Weber numbers." *J. Fluid Mech.*, 453:109–132, 2002.

[7] M. Sommerfeld. "The unsteadiness of shock waves propagating through gas-particle mixtures." *Exp. Fluids*, 3:197–206, 1985.

[8] F.E. Marble. "Dynamics of dusty gases." *Annual Review of Fluid Mechanics*, 2:397–446, 1970.

[9] Y. Tambour. "Vaporization of polydisperse fuel sprays in a laminar boundary layer flow: A sectional approach." *Combust. Flame*, 58:103–114, 1984.

[10] Y. Tambour. "A Largrangian sectional approach for simulating droplet size distribution of vaporizing fuel sprays in a turbulent jet." *Combust. Flame*, 60:15–28, 1985.

[11] Y. Tambour and S. Zehavi. "Derivation of near-field sectional equations for the dynamics of polydisperse spray flows: An analysis of the relaxation zone behind a normal shock wave." *Combust. Flame*, 95:383–409, 1993.

[12] F. Laurent and M. Massot. "Multi-fluid modelling of laminar polydisperse spray flames: origin, assumptions and comparison of sectional and sampling methods." *Combust. Theory Modelling*, 5:537–572, 2001.

[13] J.B. Greenberg, I. Silverman, and Y. Tambour. "On the origins of spray sectional conservation equations." *Combust. Flame*, 93:90–96, 1993.

[14] K. Prasad, C. Li, K. Kailasanath, C. Ndubizu, R. Ananth, and P. Tatem. "Numerical modeling of water mist suppression of methane-air diffusion flames." *Combust. Sci. and Tech.*, 132:325–364, 1998.

[15] K. Prasad, C. Li, and K. Kailasanath. "Optimizing water-mist injection characteristics for suppression of co-flow diffusion flames." *27th Symposium (Intl.) on Combustion*, pages 2847–2855, 1998.

[16] K. Prasad, C. Li, and K. Kailasanath. "Simulation of water-mist suppression of small scale methanol liquid pool fires." *Fire Safety Journal*, 33:185–212, 1999.

[17] K. Prasad, G. Patnaik, and K. Kailasanath. "Advanced Simulation Tool for Improved Damage Assessment 2) Water-Mist Suppression of Large Scale Compartment Fires." Technical Report NRL/MR/6410–00-8507, Naval Research Lab, 2000.

[18] R. Clift, J.R. Grace, and M.E. Weber. *Bubbles, Drops, and Particles*. Academic, New York, 1978.

[19] F.A. Williams. *Combustion Theory*. Addison-Wesley Publishing Company, Inc., New York, 1985.

[20] K. Prasad, C. Li, K. Kailasanath, C. Ndubizu, R. Ananth, and P. Tatem. "Numerical Modeling of Fire Suppression Using Water Mist. 1. Gaseous Methane-Air Diffusion Flames." Technical Report NRL/MR/6410–98-8102, Naval Research Lab, 1998.

[21] D.B. Spalding. *Proc. Combust. Inst.*, 4, 1953.

[22] D.B. Spalding. *Some Fundamentals of Combustion*. Butterworths, London, 1955.

[23] W.E. Ranz and W.R. Marshall. "Evaporation from drops." *Chem. Engrg. Prog.*, 48(3):141–173, 1952.

[24] J.P. Boris and D.L. Book. "Flux Corrected Transport I. SHASTA, A fluid transport algorithm that works." *J. Comput. Phys.*, 11(1):38–69, 1973.

[25] J.P. Boris, A.M. Landsberg, E.S. Oran, and J.H. Gardner. "LCPFCT—A Flux-Corrected Transport Algorithm for Solving Generalized Continuity Equations." Technical Report NRL/MR/6410–93-7192, Naval Research Lab, 1993.